J. Mech. Phys. Solids 196 (2025) 105974

Contents lists available at ScienceDirect

Journal of the Mechanics and Physics of Solids

journal homepage: www.elsevier.com/locate/jmps

Explicit topography design for complex shell structures based on embedded spline components

Wendong Huo [a], Chang Liu [a,b,*], Yilin Guo [a], Zongliang Du [a,b], Weisheng Zhang [a,b], Xu Guo [a,b,*]

[a] State Key Laboratory of Structural Analysis, Optimization and CAE Software for Industrial Equipment, Department of Engineering Mechanics, International Research Center for Computational Mechanics, Dalian University of Technology, Dalian 116023, PR China
[b] Ningbo Institute of Dalian University of Technology, Ningbo 315016, PR China

ARTICLE INFO

Keywords:
Shell structures
Topography optimization
Moving morphable components (MMC)
Computational conformal mapping (CCM)

ABSTRACT

The slender property of shell structures causes the magnitude difference between in-plane and out-of-plane stiffness. Inspired by such a geometry-induced anisotropy phenomenon, this paper proposes a novel design approach to improve the stiffness of complex shell structures. The optimization algorithm is constructed based on two technical pillars, i.e., the explicit moving morphable components (MMC) framework and the computational conformal mapping (CCM) technique. Owing to the MMC framework, the proposed approach can describe complex topography fields with local details via relatively few design variables, theoretically decreasing the computation burden. Towards shell structures in practice, of which the geometry models are usually flexible and complex, we leverage the CCM technique to parameterize the middle surfaces to obtain a unified and robust algorithm architecture. Representative examples with complex geometry models are provided to validate the proposed design method's effectiveness, efficiency, and universality.

1. Introduction

Shell structure is one of the most ubiquitous and efficient structural elements in nature and engineering. Examples include cell (Banigan et al., 2017; Lim et al., 2002), microcapsule (Gordon et al., 2004), bionics (Wu et al., 2024), architecture (Adriaenssens et al., 2014), automobile (Zhang et al., 2006), and spacecraft (Pisacane, 2005), etc. The superb performance of shell structures primarily arises from their slender, curved geometry, which enables them to effectively bear external loads while providing efficient protective capabilities (Chapelle and Bathe, 2011). However, shell structures usually suffer from extreme service environments and complicated loading conditions in practical applications. Consequently, the design of shell structures has long been a significant research focus, owing to the ability to further improve its load-bearing performance and economic benefit. Many works have emerged in this context, falling into four distinct categories: size optimization, shape optimization, topology optimization, and stiffening rib optimization.

Size optimization of a shell structure is straightforward, i.e., altering the specific geometric sizes such as height, width, and thickness. Shape optimization encompasses two techniques: CAD-based methods (Agarwal et al., 2019; Kang and Youn, 2016; Xu et al., 2014) and node-based methods (Antonau et al., 2022; Hojjat et al., 2014; Shimoda and Liu, 2014). CAD-based methods utilize the spline models, particularly NURBS descriptions for free surfaces (Piegl and Tiller, 2012), to represent shell structures, with design

* Corresponding authors.
E-mail addresses: c.liu@dlut.edu.cn (C. Liu), guoxu@dlut.edu.cn (X. Guo).

https://doi.org/10.1016/j.jmps.2024.105974
Received 26 July 2024; Received in revised form 6 November 2024; Accepted 24 November 2024
Available online 25 November 2024

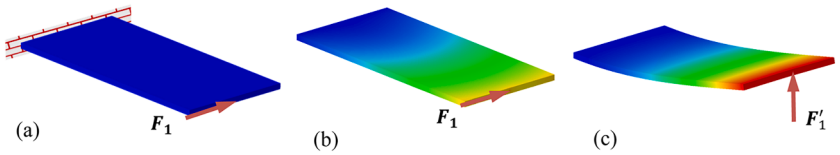

Fig. 1. Schematic illustration of the stiffness difference induced by the slenderness property. (a) A shell structure of linear isotropic elastic material is fixed at the end, and subjected to an in-plane static load. (b) The resultant displacement of (a) is in-plane-dominated. (c) The force is rotated to the vertical direction, and then the displacement pattern of the shell structure is changed to out-of-plane deformation dominated. These two cases show that the in-plane stiffness is much larger than the out-of-plane stiffness for shell structures.

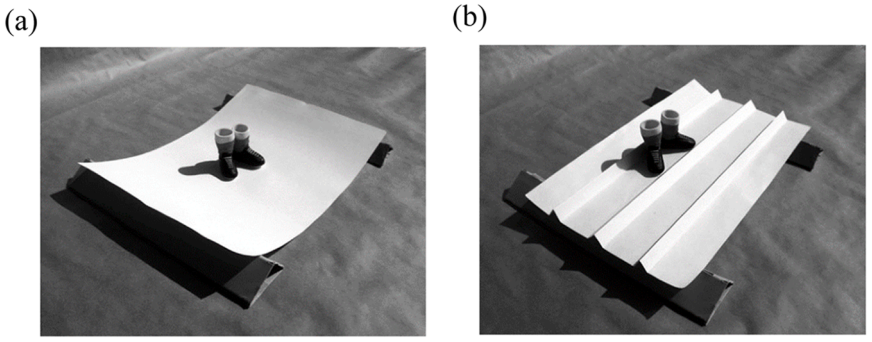

Fig. 2. Topography variation can be exploited to modify the load-bearing mode of shell structures and enhance structure performances. (a-b) A representative example of leveraging topography variation to modify the load-bearing mode (Adriaenssens et al., 2014). (a) The flat plate is easily bended under the load. (b) In the form of reinforcing ribs, the uneven topography makes the structure more resistant to bending.

objects being the corresponding modeling parameters. Unlike size optimization, the design objects in CAD-based methods control the shape but do not represent specific geometric sizes. On the other hand, node-based methods, also known as vertex-based or CAD-free methods, exploit the coordinates of the nodes in finite element discretization as the design variables. Research on topology optimization of shell structures dates back to the pioneering work (Cheng and Olhoff, 1981). Since then, various powerful methods have been exploited to conduct topology optimization for shell structures, including the Solid Isotropic Material with Penalization (SIMP) method (Maute and Ramm, 1997), the Bi-directional Evolutionary Structural Optimization (BESO) method (Xiong et al., 2023), the Level Set Method (LSM) (Townsend and Kim, 2019), and the Moving Morphable Components (MMC) method (Huo et al., 2022). Among these, topology optimization for shell structures based on the MMC method (Guo et al., 2014) can achieve final results with clear load paths using a small number of design variables, owing to the design variables endowed with geometric meanings. In contrast, stiffener optimization focuses on the attached stiffening ribs rather than the shell structure. Rib-stiffened shells have been widely researched due to their convenient and efficient properties in various scenarios. Examples include designing stiffeners with casting constraints (Liu et al., 2015), optimizing hierarchical stiffened shells based on the Smeared Stiffener Method (SSM) to reduce computational burden (Hao et al., 2014), solving layout optimization problems for curved stiffeners on composite shell structures (Wang et al., 2019), and using B-spline parameterization to optimize stiffener layout for shell structures (Feng et al., 2021). Additionally, these approaches are not strictly independent. Many integrated design approaches have been proposed to enhancing structural performance further. Examples include shape and topology optimization of shell structures (Ansola et al., 2002; Cai et al., 2023; Hassani et al., 2013), using topology optimization to design stiffening ribs (Jiang et al., 2022, 2023), concurrently optimizing the shape of shell structures and the layout of attached reinforcement ribs (Ansola et al., 2004), unified frameworks (Huo et al., 2023), and simultaneously optimizing the topology and layout of stiffeners on shells (Bakker et al., 2021).

In summary, various design methods emphasize different aspects. Size and shape optimizations focus on adjusting modeling parameters. Topology optimization, on the other hand, aims to eliminate inefficient or ineffective material (such as low-strain-energy elements in static compliance optimization) and distribute material efficiently to achieve lightweight designs. The success of rib-stiffened structures lies in the ability of attached stiffeners to enhance out-of-plane stiffness and mitigate detrimental out-of-plane deformation. In contrast to the existing approaches, the current study stems from observing the load-bearing nature of shell structures. Specifically, the inherent slenderness property of shell geometry induces stiffness difference along different directions (as depicted in Fig. 1). Given this geometry-induced anisotropy, we introduce topography variation as a specialized structural element to modify the load-bearing mode. As shown in Fig. 2, the uneven topography increases the structure stiffness by transforming the flat, flexible plate into a wavy form. Analogous to reinforcing ribs, the shell topography can improve structure performance by restraining global out-of-plane deformation.

The effects of topography on structural responses have been studied across different scales and disciplines, such as geometry-induced rigidity (Lazarus et al., 2012), wave motion (Dorn and Kochmann, 2023), metamaterials (Faber et al., 2020), crystallography (Vitelli et al., 2006), and crack manipulation (Feng et al., 2023; Liu et al., 2023; Mitchell et al., 2017). However, these studies

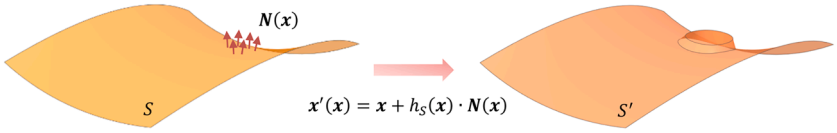

Fig. 3. The topography variation is realized via the surface perturbation. The perturbation direction is along the positive normal vector of each point of the original surface. Nevertheless, constructing the topography function in a pointwise manner will involve complicated surface operations.

have focused on the forward problem of exploring underlying mechanical mechanisms. From a mathematical and technological perspective, a more interesting question is the inverse problem of designing topography variation that achieve superior or prescribed structure properties. Several critical issues emerge when addressing the challenge of designing topography for curved shell structures: how to describe topography on general surface shells, parameterize the complicated topography variation, and construct an optimization formulation to drive the design process? In response, we propose a systematical topography optimization method that tackles these challenges and obtains rational designs. The cornerstone of this approach is the so-called embedded spline components, which embeds spline-based MMC components from a simple plane domain into the original complex surface using the computational conformal mapping (CCM) technique. Benefiting from the explicit MMC framework (Guo et al., 2014; Zhang et al., 2016), spline components can achieve complex topography descriptions with a small number of design variables. On the other hand, the CCM technique (Lui et al., 2014, 2013; Meng et al., 2016) maps the middle surface to a standard plane domain, enabling the approach to handle shell structures with complex geometry.

From the algorithmic perspective, the proposed approach is a generalized shape optimization method, and its advantages are summarized below. The MMC method describes complex topographic variations using a few spline-based components, significantly reducing the number of design variables. The reduction in variable number directly lowers the computational cost of the optimization problem, especially when compared to node-based methods, which require a much larger number of variables corresponding to the number of nodes. Computational efficiency is further enhanced by conformal mapping, simplifying the handling process of complex geometries. This technique transforms the complex shell surface into a simpler parameter domain, allowing the MMC-based optimization to be performed more effectively. It also eliminates the need for the tedious re-meshing processes commonly required in CAD-based methods. Moreover, our approach utilizes a mesh model to represent the geometry, avoiding the initial parameterization for the middle surface of the shell and extensive re-parameterizations for topographic details, as required in CAD-based approaches. The method naturally produces smooth topographies, eliminating the need for the filtering steps often required at each iteration in node-based approaches. Additionally, our method is compatible with previous techniques and can be combined to create more efficient structures. This study gives special consideration to the topography design of shell structures with complex geometry models.

This article is structured as follows. Section 2 introduces the theoretical foundations of constructing embedded spline components. In Section 3, the optimization problem is formulated, and the detailed sensitivity analysis is derived. Section 4 describes specific solution techniques and design processes. In Section 5, a series of numerical experiments are conducted to explore the effects of parameters on improving structural performance, and several representative design examples are provided to validate the effectiveness and efficiency of the proposed method. Conclusions and extensions are presented in the final section.

2. Theoretical foundations

This section briefly outlines the approach to constructing topography variation based on the MMC framework, which is subsequently utilized to alter the shape of shell structures.

2.1. Embedded topography description

In this study, we utilize the middle-surface approach to modeling the shell structure. The configuration of surface S, representing the middle surface of the shell structure to be designed, is perturbed by the topography variation. Specifically, for each point $\boldsymbol{x}$ on the surface S, its position is moved to $\boldsymbol{x}'(\boldsymbol{x})$ along the direction of the positive normal vector $\boldsymbol{N}(\boldsymbol{x})$ via

$$\boldsymbol{x}'(\boldsymbol{x}) = \boldsymbol{x} + h_S(\boldsymbol{x}) \cdot \boldsymbol{N}(\boldsymbol{x}), \tag{2.1}$$

where $h_S(\boldsymbol{x})$ is the *surface topography field (STF) function* reflecting the variation magnitude, as shown in Fig. 3. The normal vector is defined through classical differential geometry for smooth surfaces and discrete differential geometry (Taubin, 1995) for unsmooth cases. Constructing such a pointwise function will involve complicated surface operations and lead to problems when extended to arbitrary complex shell models. In this context, we propose the embedded topography description, which maps the middle surface to a standard parametric domain first, defines the topography function in the obtained parametric domain, and embeds the topography into the middle surface in the end.

Mapping a complex surface to a simple domain, known as surface parameterization, plays a crucial role in computer industries (Kuo et al., 2021). Many significant tasks, including texture mapping, surface morphing, and mesh generation, rely on the dimension-reduction property of surface parameterization (Gu et al., 2004). Due to the rapid development in computer science, numerous innovative methods (Jin et al., 2008; Kharevych et al., 2006; Su et al., 2016) have been developed and implemented to

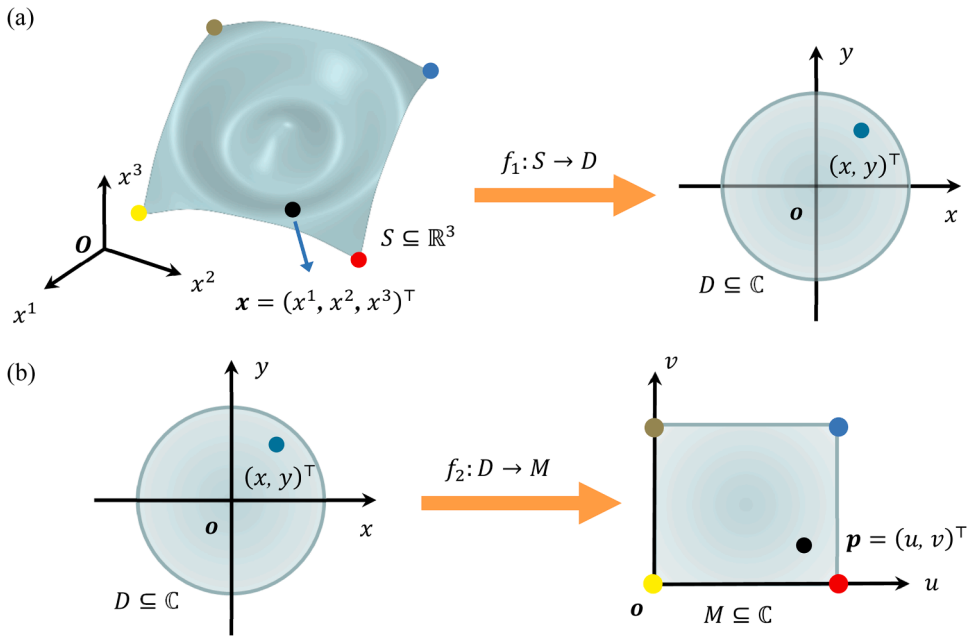

Fig. 4. Schematic illustration of solving the conformal mapping by composing two quasi-conformal mappings. (a) The first mapping. (b) The second mapping.

achieve surface parameterization. The proposed study utilizes the computational conformal mapping technique (Lui et al., 2014, 2013; Meng et al., 2016) to acquire proper mappings, where the advantages of bijectivity and conformality are fundamental to alleviating nonlinearity and singularity in the optimization problem formulation. The primary task of the CCM technique is computing a conformal mapping $f : S \to M$, where M is a rectangular parametric domain defined in $\mathbb{R}^2$. Here, S is restricted to homeomorphic to M. Instead of directly computing the mapping, we achieve conformality by composing two quasi-conformal mappings with appropriate Beltrami coefficients, significantly accelerating the computation. The first quasi-conformal mapping $f_1 : S \to D \subset \mathbb{C}$ is a disk harmonic mapping obtained by solving the following equations using the finite element method (Pinkall and Polthier, 1993):

$$\begin{cases} \Delta_S f_1 = 0, \ \text{in } S, \\ f_1(\partial S) = \partial D, \end{cases} \tag{2.2}$$

where Δ_S is the Laplace-Beltrami operator defined on the surface S, the symbol D represents the target disk domain defined in the complex plane $\mathbb{C}$ (see Fig. 4(a)), and symbols ∂S and ∂D represent the boundaries of S and D, respectively. Then, the linear Beltrami solver (LBS) scheme (Lui et al., 2014) is leveraged here to eliminate the conformality distortion of the first mapping. Denote $\mu_{f_1^{-1}} = \rho + j\tau$ the Beltrami coefficient of the inverse mapping f_1^{-1} with ρ, τ, and j representing the real part, the imaginary part, and the imaginary unit ($j^2 = -1$), respectively. Let $f_2(x+jy) = u(x,y) + jv(x,y) : D \to M$ be the second desired quasi-conformal mapping (see Fig. 4(b)), whose Beltrami coefficient is given by $\mu_{f_2} = \mu_{f_1^{-1}}$. Here, (x,y) and (u,v) are the complex coordinates defined on the disk D and the parameter domain M, respectively. According to the LBS scheme, the mapping f_2 can be reconstructed by solving the following system of equations (also realized through the finite element method):

$$\begin{cases} \nabla \cdot (\mathbf{A}(\nabla u)) = 0, \ \text{in } D, \\ \nabla \cdot (\mathbf{A}(\nabla v)) = 0, \ \text{in } D, \\ f_2(\partial D) = \partial M, \end{cases} \tag{2.3}$$

where $\nabla(\cdot) = \left(\frac{\partial(\cdot)}{\partial x}, \frac{\partial(\cdot)}{\partial y}\right)$, $\mathbf{A} = \begin{pmatrix} \alpha_1 & \alpha_2 \\ \alpha_2 & \alpha_3 \end{pmatrix}$ with $\alpha_1 = \frac{(\rho-1)^2+\tau^2}{1-\rho^2-\tau^2}$, $\alpha_2 = -\frac{2\tau}{1-\rho^2-\tau^2}$, and $\alpha_3 = \frac{(\rho+1)^2+\tau^2}{1-\rho^2-\tau^2}$. Here, ∂M represents the boundary of the rectangular domain M. The ultimate mapping f is established as $f = f_2 \circ f_1$. By leveraging the resultant mapping of the conformal parameterization process, the definition domain of the STF function is reduced to the parametric domain M, i.e.,

$$h_S(\boldsymbol{x}) = h_S(f^{-1}(\boldsymbol{p})) = h_M(\boldsymbol{p}), \tag{2.4}$$

with $f(\boldsymbol{x}) = \boldsymbol{p}(u,v)$ and h_M representing the *plane topography field (PTF) function*. Furthermore, the perturbation of the surface is modified as

$$\boldsymbol{x}'(\boldsymbol{x}) = \boldsymbol{x} + h_M(\boldsymbol{p}) \cdot \boldsymbol{N}(\boldsymbol{x}), \tag{2.5}$$

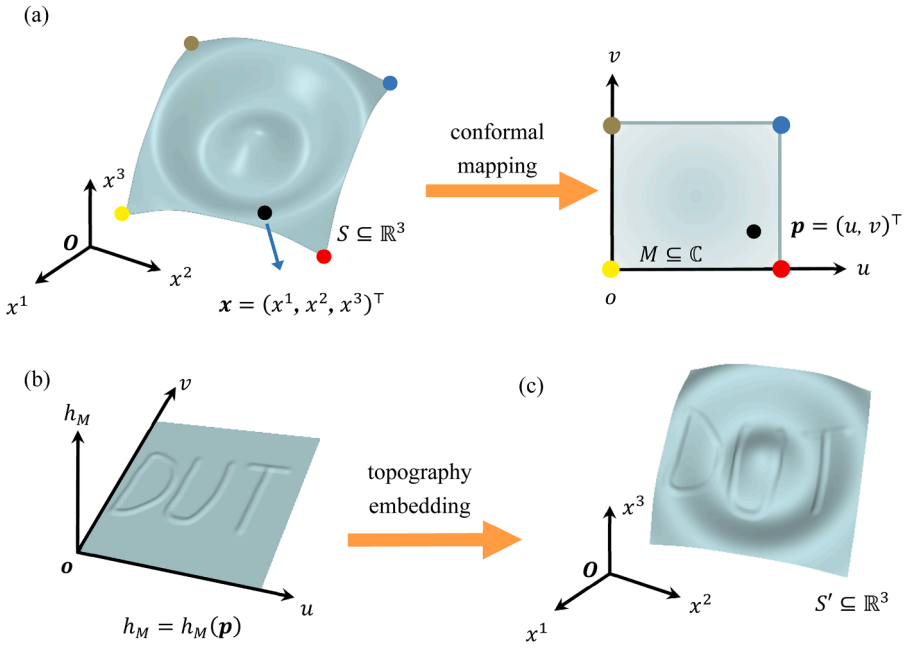

Fig. 5. Schematic illustration of the implementation process of the embedded topography description. (a) The first step is to solve the conformal mapping and obtain the parametric domain via the CCM technique. (b) Designing topography variation (the DUT letters) in the parametric domain. (c) Embedding the topography design into the original surface, i.e., Eq. (2.5).

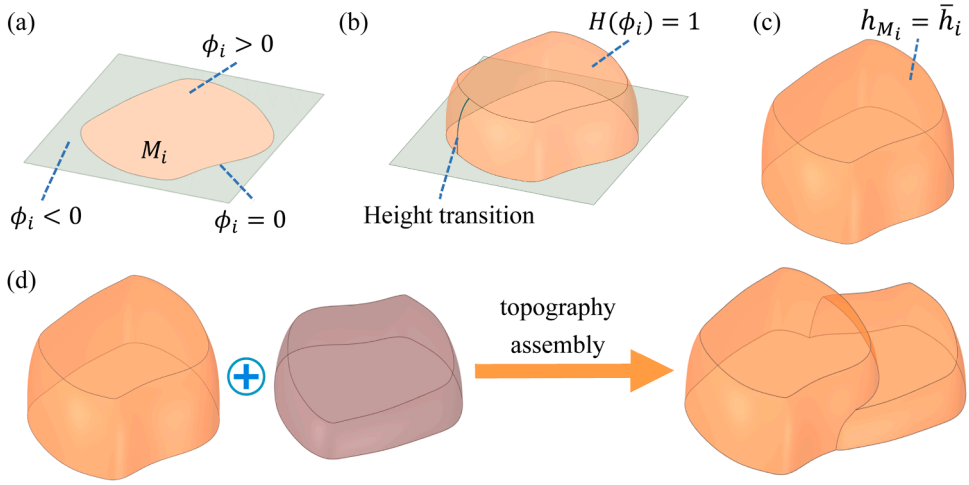

Fig. 6. Schematic illustration of the construction process of the PTF function. (a) The TDF function ϕ_i indicates the perturbation domain. (b) The Heaviside function is leveraged to regularize the height value. (c) The topography magnitude is scaled by the height design variable. (d) The global plane topography function is constructed via the topography assembly process, i.e., Eq. (2.8).

which means that for each point $\boldsymbol{x}$, the construction process of perturbation magnitude is simplified from the surface S to the plane domain M under the embedded topography description framework, as shown in Fig. 5.

2.2. Construction strategy of the plane topography field (PTF) function

Analogous to structure topology optimization (Guo et al., 2014), the moving morphable components (MMC) method is introduced to approximate the optimal plane topography function, $h_M(\boldsymbol{p})$. The complex and continuously varying topography comprises a set of moving, morphing, and merging structure components, which makes the proposed algorithm possess the advantages of a small number of design variables, clear and smooth structure boundaries, and interpretable final designs. Specifically, this study leverages the topology description function (TDF) to characterize the perturbed domain. For the i-th component, its TDF is expressed as

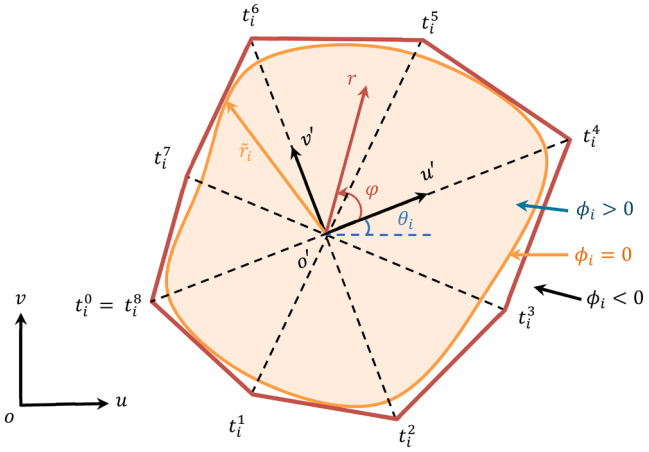

Fig. 7. Schematic illustration of a spline component with $nr = 8$.

$$\begin{cases} \phi_i(u,v) > 0, \text{ if } (u,v) \in M_i, \\ \phi_i(u,v) = 0, \text{ if } (u,v) \in \partial M_i, \\ \phi_i(u,v) < 0, \text{ if } (u,v) \in M \setminus (M_i \cup \partial M_i), \end{cases} \tag{2.6}$$

where M_i is a subset of the parametric domain M occupied by the i-th component (shown in Fig. 6(a)), and ∂M_i represents the boundary of M_i. Note that the TDF function only indicates whether the domain is protuberant and the height information is missing. Hence, as displayed in Fig. 6(b-c), the topography field is further constructed as

$$h_i(u,v) = \overline{h}_i \cdot H(\phi_i(u,v)), \tag{2.7}$$

where the symbol $\overline{h}_i$, as a design variable, represents the height of the i-th topography component, and $H(\cdot)$ is the regularization Heaviside function (Zhang et al., 2016) that maps the variable to the interval of $[0,\ 1]$. At the global level (illustrated in Fig. 6(d)), the plane topography function h_M consists of the topography field function of every component:

$$h_M = \max(h_1, \ldots, h_i, \ldots, h_{nc}), \tag{2.8}$$

where nc represents the total number of components in the design domain.

2.3. Spline component description for topography function

In contrast to the TDF constructions in previous studies (Zhang et al., 2016), this paper proposes a novel spline component description to efficiently parameterize topography functions. This description is capable of describing complex surface topography with a small number of variables. It is noteworthy that the complexity of topography arises not only from height variations, which can be addressed using Eq. (2.7-2.8), but also from the shape of the boundary of the perturbed domain. Therefore, the indicative function $\phi_i(u,v)$ requires careful definition. To address these challenges, we employ the spline component to describe the shape of the perturbation domain, as illustrated in Fig. 7. First of all, we construct a local coordinate system $(u',\ v')$ by

$$\begin{pmatrix} u' \\ v' \end{pmatrix} = \begin{bmatrix} \cos\theta_i & \sin\theta_i \\ -\sin\theta_i & \cos\theta_i \end{bmatrix} \begin{pmatrix} u - u_0^i \\ v - v_0^i \end{pmatrix}, \tag{2.9}$$

where u_0^i and v_0^i are the local coordinates of the i-th component's central point, and θ_i represents its rotational angle with respect to the global Cartesian coordinate system. These three design variables, u_0^i, v_0^i, and θ_i endow the component with the capacity of rigid displacement. In the second place, we transfer the Cartesian coordinate system to a polar coordinate (r, φ) by

$$r = \sqrt{(u')^2 + (v')^2}, \tag{2.10}$$

$$\varphi = \arctan\left(\frac{v'}{u'}\right). \tag{2.11}$$

Then, the boundary of the i-th component is expressed by the radius-basis form:

$$\tilde{r}_i(\varphi) = \sum_{k=0}^{nr} R_{k,p}(\varphi) t_i^k, \tag{2.12}$$

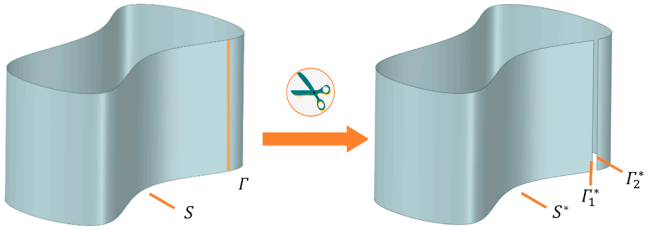

Fig. 8. STFF definition via the surface-cutting operation.

where t_i^k is the k-th shape coefficient of the i-th component (t_i^0 equals t_i^{nr} such that the boundary forms a closed loop), and $R_{k,p}$ is the p-order ($p = 2$ in this study) NURBS radius basis function and has the following form:

$$R_{k,p}(\varphi) = \frac{N_{k,p}(\varphi) w_k}{\sum_{l=0}^{nr} N_{l,p}(\varphi) w_l}. \tag{2.13}$$

In Eq. (2.13), w_k is the weight associated with the k-th basis function ($w_k = 1$ in this study), and $N_{k,p}(\varphi)$ is the k-th B-spline basis function defined by the Cox-de Boor recursion formula:

$$N_{k,0}(\varphi) = \begin{cases} 1, & \text{if } \varphi^k \le \varphi \le \varphi^{k+1}, \\ 0, & \text{otherwise}, \end{cases} \tag{2.14}$$

and

$$N_{k,p}(\varphi) = \frac{\varphi - \varphi^k}{\varphi^{k+p} - \varphi^k} N_{k,p-1}(\varphi) + \frac{\varphi^{k+p+1} - \varphi}{\varphi^{k+p+1} - \varphi^{k+1}} N_{k+1,p-1}(\varphi), \ p \ge 1 \tag{2.15}$$

where φ^k is the k-th knot belongs to the knot vector $\Xi = \left\{\varphi^1, \varphi^2, \ldots, \varphi^{nr+p+1}\right\}$. At last, the indicative function $\phi_i(u, v)$ is defined via a regularized form:

$$\phi_i(u, v) = 1 - \left(\frac{r}{\widetilde{r}_i(\varphi) + eps}\right)^q. \tag{2.16}$$

where the symbol q represents the shape exponent ($q = 2$ in this study), and $eps = 10^{-15}$ is a tiny quantity that prevents singularity. Owing to the strong deformation capacity of the NURBS description, the definition (2.16) can easily characterize the complex shape of the perturbation domain. On the other hand, the local-support property of the spline basis function circumvents potential Runge's phenomenon in shape interpolation, i.e., Eq. (2.12). Further, it ensures numerical stability in the optimization process. In conclusion, the vector of the design variables of the i-th spline-based component is defined as $\boldsymbol{D}_i = \left(u_0^i, v_0^i, \theta_i, t_i^1, t_i^2, \ldots, t_i^{nr}, \overline{h}_i\right)$, and the vector of the design variables of the global topography description is assembled as $\boldsymbol{D} = (\boldsymbol{D}_1, \boldsymbol{D}_2, \ldots, \boldsymbol{D}_n)$. The topography function is thereby defined as $h_S(\boldsymbol{x}; \boldsymbol{D}) = h_M(\boldsymbol{p}; \boldsymbol{D})$.

2.4. Topography definition on arbitrary complex surfaces

In the sections above, we have proposed detailed construction procedures to obtain the topography function. An underlying hypothesis of the CCM technique we utilized may be overlooked: the original surface should be homeomorphic to a rectangle domain, which limits the algorithm application scope. Considering the potential geometric complexity of the shell structure, two additional solutions are introduced in this section, i.e., the surface-cutting operation and the multi-patch stitching scheme, to handle surfaces with complex topology properties and enhance the practicability of the proposed design method.

2.4.1. Surface topography field (STF) function definition via the surface-cutting operation

When the middle surface of the designed shell structure possesses non-trivial topology (e.g., multi-connected, non-zero genus, etc.), the CCM technique mentioned above and the approaches to constructing the surface topography field cannot be used directly. In this context, the surface-cutting operation is introduced to preprocess the original surface. Taking the cylinder model as an example, as illustrated in Fig. 8, we first cut along the generatrix Γ (for arbitrary manifold surfaces, the cut lines are obtained through algorithms of computational topology (Dey et al., 2008)), after which the intermediate surface S^* is generated. The surface S^* is topologically equivalent to a plane rectangle; that is, the conformal mapping $f : S^* \to M$ can be obtained via the CCM technique, where M represents the corresponding parametric domain. Concerning the topography function of the surface S^*, the construction follows the rules in the preceding sections, i.e., $h_{S^*}(\boldsymbol{x}^*; \boldsymbol{D}) = h_M(\boldsymbol{p}; \boldsymbol{D})$ where symbols $\boldsymbol{x}^*$ and $\boldsymbol{p}$ represent the point on the surface S^* and the corresponding point that is mapped to the parameter domain, respectively. Note that the curve Γ on the original surface S derives two curves Γ_1^* and Γ_2^* on S^*; that is, for each point $\boldsymbol{x} \in \Gamma$, it splits into two points $\boldsymbol{x}_1^*$ and $\boldsymbol{x}_2^*$, which further causes inconsistency of the topography function h_S

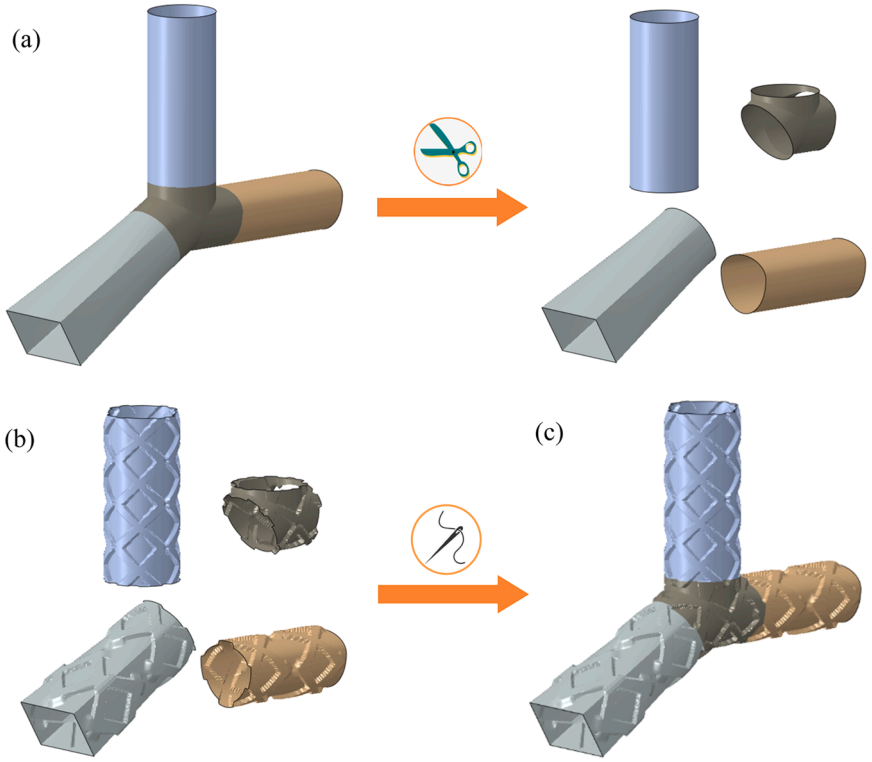

Fig. 9. STFF definition via the multi-patch stitching scheme. (a) The original surface is divided into four patches according to the geometry feature. (b) The topography of each patch is constructed via the approaches above, which include the embedded description and the surface-cutting operation. (c) The topography of the whole surface is obtained by stitching all patches with defined topography.

taken on the cutting curve Γ. Back to the original surface S, the topography function h_S is therefore defined as:

$$h_S(\boldsymbol{x};\boldsymbol{D}) = \begin{cases} h_{S^*}(\boldsymbol{x}^*;\boldsymbol{D}), \ \text{if } \boldsymbol{x} \in \ S \setminus \Gamma, \\ \max\left(h_{S^*}\left(\boldsymbol{x}_1^*;\boldsymbol{D}\right), h_{S^*}\left(\boldsymbol{x}_2^*;\boldsymbol{D}\right)\right), \ \text{if } \boldsymbol{x} \in \Gamma. \end{cases} \tag{2.17}$$

2.4.2. Surface topography field (STF) function definition via the multi-patch stitching scheme

Up to now, the proposed method has been able to deal with general complex surfaces. However, due to the global property, the single-mapping process may involve numerical instabilities. Hence, the multi-patch stitching scheme is introduced to address this issue, which decomposes the original complex surface into several simple patches according to geometry features, and then defines topography functions in these relatively simple surface patches, and stitches perturbed patches together at last, as demonstrated in Fig. 9. Similar to the former subsection, further treatments are required after the decomposition. Suppose $S = \cup_{i=1}^{ns} S_i$ is a surface partition, where S_i is the i-th surface patch, and ns is the number of patches. Note that no shape constraint of each patch is required. For each patch S_i, the topography field is characterized as h_{S_i}, which is computed through Eqs. (2.4, 2.6-2.17). For the sake of defining the topography of the whole surface, the locally defined topography function h_{S_i} is extended to the global domain by:

$$h_{S_i}^{\mathrm{s}}\left(\boldsymbol{x};\boldsymbol{D}^i\right) = \begin{cases} h_{S_i}\left(\boldsymbol{x};\boldsymbol{D}^i\right), \ \text{if } \boldsymbol{x} \in S_i, \\ 0, \ \text{if } \boldsymbol{x} \notin S_i, \end{cases} \tag{2.18}$$

where $\boldsymbol{D}^i$ is the vector of design variables corresponding to the patch S_i. In Eq. (2.18), 0 represents no perturbation defined out of domain S_i. By leveraging the extended definition, the topography function of the whole surface is assembled as follows:

$$h_S(\boldsymbol{x};\boldsymbol{D}) = \max\left(h_{S_1}^{\mathrm{s}}, h_{S_2}^{\mathrm{s}}, \ldots, h_{S_{ns}}^{\mathrm{s}}\right). \tag{2.19}$$

3. Problem statement and sensitivity analysis

3.1. Optimization formulation

In this study, we consider the topography optimization problem that minimizes the structural compliance of shell structures. All

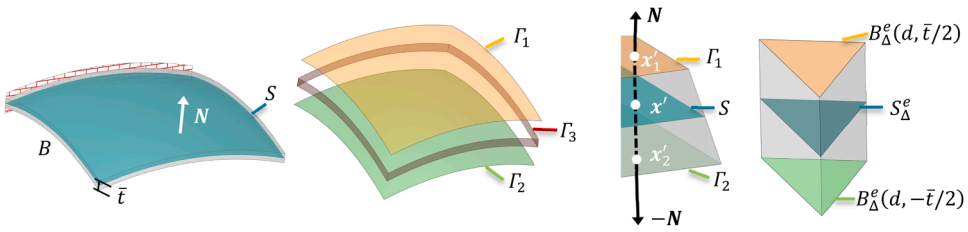

(a) bulk and middle surface (b) boundary decomposition (c) point projection (d) discrete bulk

Fig. 10. (a) Schematic illustration of the relationship of the middle surface with the bulk domain. (b) The boundary of the bulk domain is decomposed into three parts. (c) The thickness and the curvature give rise to the velocity inconsistency between the upper surface and the lower surface, hence points on these two surfaces are considered separately. (d) Representation of the bulk domain in the discrete level.

materials involved are assumed to be linear elastic, isotropic, and homogenous. Suppose $S(\boldsymbol{D})$ is the perturbed middle surface of the shell structure. We have $S_0 = S(\boldsymbol{0})$ representing the original middle surface and $B(\boldsymbol{D}, t) = S(\boldsymbol{D}) \times [-\bar{t}/2, \bar{t}/2]$ representing the domain occupied by the perturbed shell structure, where t is the thickness coordinate, and $\bar{t}$ is the thickness of the shell. In contrast to that the middle surface S is the core concern for geometric modeling in the previous section, this section mainly focuses on the bulk domain considering the shell theory utilized (shown in Fig. 10(a)). The topography optimization problem under the current spline-component-based framework is formulated as

$$\text{Find } \boldsymbol{D},\ \boldsymbol{U}(\boldsymbol{x};\boldsymbol{D}) \tag{3.1a}$$

$$\text{Minimize } C = C(\boldsymbol{U}(\boldsymbol{x};\boldsymbol{D}), \boldsymbol{D}) = \int_{B(\boldsymbol{D},t)} (\boldsymbol{F}(\boldsymbol{D}) \cdot \boldsymbol{U}(\boldsymbol{x};\boldsymbol{D}))\mathrm{dV}, \tag{3.1b}$$

$$\text{s.t.} \int_{B(\boldsymbol{D},t)} \left(\mathscr{C}^{\alpha\beta\lambda\mu} e_{\alpha\beta}(\boldsymbol{U}(\boldsymbol{x};\boldsymbol{D})) e_{\lambda\mu}(\boldsymbol{V}(\boldsymbol{x};\boldsymbol{D})) + \mathscr{D}^{\alpha\lambda} e_{\alpha 3}(\boldsymbol{U}(\boldsymbol{x};\boldsymbol{D})) e_{\lambda 3}(\boldsymbol{V}(\boldsymbol{x};\boldsymbol{D})) \right) \mathrm{dV} = \int_{B(\boldsymbol{D},t)} (\boldsymbol{F}(\boldsymbol{D}) \cdot \boldsymbol{V}(\boldsymbol{x};\boldsymbol{D}))\mathrm{dV},\ \forall\ \boldsymbol{V}(\boldsymbol{x};\boldsymbol{D}) \in U_{ad}, \tag{3.1c}$$

$$\boldsymbol{U}(\boldsymbol{x};\boldsymbol{D}) \in U,\ \boldsymbol{D} \in \mathscr{U}_{\boldsymbol{D}}, \tag{3.1d}$$

where the symbols C and $\boldsymbol{F}(\boldsymbol{D})$ represent the structural compliance function and the external force, respectively, $\mathscr{C}^{\alpha\beta\lambda\mu}$ and $\mathscr{D}^{\alpha\lambda}$ are the constitutive tensors of the curvilinear coordinate system. In Eq. (3.1), the primary displacement $\boldsymbol{U}(\boldsymbol{x};\boldsymbol{D})$ belongs to a prescribed constraint set U, and the virtual displacement $\boldsymbol{V}(\boldsymbol{x};\boldsymbol{D})$ belongs to an admissible set U_{ad}. These two displacements both satisfy the Reissner-Mindlin kinematical assumption. Additionally, $e_{\alpha\beta}(\cdot)$ is the surface strain tensor (containing the membrane and bending behaviors), $e_{\alpha 3}(\cdot)$ is the transverse shear strain tensor, and $\mathscr{U}_{\boldsymbol{D}}$ is the set utilized to avoid infeasible topography descriptions.

3.2. Sensitivity analysis

As shown in Eq. (3.1), the integral domain of structural responses (i.e., $B(\boldsymbol{D},t)$) varies during the design processes. Hence, we utilize the shape sensitivity analysis method to handle the shape variation (Choi and Kim, 2004; Sokolowski and Zolesio, 1992). For the sake of simplicity of illustration, we use the symbol d, which is an arbitrary element of design variables, to represent the parameter controlling the shell shape instead of the vector $\boldsymbol{D}$. Suppose $I(W) = \int_{B(d,t)} W\mathrm{dV}$ is a general structural response (assuming that $I(W)$ satisfies the design domain's regularity requirements and some smoothness conditions), where $W = W(\boldsymbol{U}(\boldsymbol{x};d),\ \boldsymbol{V}(\boldsymbol{x};d))$ is a functional of $\boldsymbol{U}(\boldsymbol{x};d)$ and $\boldsymbol{V}(\boldsymbol{x};d)$. Here, $\boldsymbol{U}(\boldsymbol{x};d)$ and $\boldsymbol{V}(\boldsymbol{x};d)$ are displacements corresponding to $\boldsymbol{U}(\boldsymbol{x};\boldsymbol{D})$ and $\boldsymbol{V}(\boldsymbol{x};\boldsymbol{D})$, respectively. According to Raynold's transport theorem, the material time derivative of $I(W)$ is

$$\frac{\mathrm{D}}{\mathrm{D}d} I(W) = \int_{B(d,t)} \left(\frac{\partial W}{\partial d} + \mathrm{div}(W\boldsymbol{v}) \right) \mathrm{dV}, \tag{3.2}$$

where $\mathrm{div}(\cdot)$ is the divergence operator, and the symbol $\boldsymbol{v}$ is the velocity field induced by the instant change of the parameter d. By leveraging the Gauss theorem, the second term in Eq. (3.2) is reduced to the boundary $\partial B(d,t)$ as

$$\int_{B(d,t)} \mathrm{div}(W\boldsymbol{v})\mathrm{dV} = \int_{\partial B(d,t)} WV_n \mathrm{dS}, \tag{3.3}$$

where $V_n = \boldsymbol{v} \cdot \boldsymbol{N}$ with $\boldsymbol{N}$ representing the outer normal vector defined on $\partial B(d,t)$, and we have

$$\frac{\mathrm{D}}{\mathrm{D}d} I(W) = \int_{B(d,t)} \left(\frac{\partial W}{\partial d} \right) \mathrm{dV} + \int_{\partial B(d,t)} WV_n \mathrm{dS}. \tag{3.4}$$

Below, we conduct the specific sensitivity analysis according to the above formula. We denote by $W_C = W_C(\boldsymbol{U}(\boldsymbol{x};d), \boldsymbol{V}(\boldsymbol{x};d))$ the integrand of the left-hand side of Eq. (3.1c), i.e., the generalized density of strain energy, we have

$$\frac{\partial W_C(\boldsymbol{U}(\boldsymbol{x};d),\ \boldsymbol{V}(\boldsymbol{x};d))}{\partial d} = W_C(\boldsymbol{U}'(\boldsymbol{x};d), \boldsymbol{V}(\boldsymbol{x};d)) + W_C(\boldsymbol{U}(\boldsymbol{x};d), \boldsymbol{V}'(\boldsymbol{x};d)), \tag{3.5}$$

where $(\cdot)' = \frac{\partial}{\partial d}(\cdot)$ represents the local derivative. According to Eq. (3.4), the material time derivative of the left-hand side of Eq. (3.1c) is given by

$$\frac{\mathrm{D}}{\mathrm{D}d} I(W_C) = \int_{B(d,t)} (W_C(\dot{\boldsymbol{U}}(\boldsymbol{x};d), \boldsymbol{V}(\boldsymbol{x};d)) + W_C(\boldsymbol{U}(\boldsymbol{x};d), \dot{\boldsymbol{V}}(\boldsymbol{x};d)))\mathrm{dV} + \int_{\partial B(d,t)} W_C V_n \mathrm{dS} \tag{3.6}$$

Denote the integrand of the right-hand side of Eq. (3.1c) by $W_F = W_F(\boldsymbol{U}(\boldsymbol{x};d),\ \boldsymbol{V}(\boldsymbol{x};d))$, we have

$$\frac{\mathrm{D}}{\mathrm{D}d} I(W_F) = \int_{B(d,t)} \left(\frac{\partial W_F}{\partial d}\right)\mathrm{dV} + \int_{\partial B(d,t)} W_F V_n \mathrm{dS}, \tag{3.7}$$

where $W_F = \boldsymbol{F}(d) \cdot \boldsymbol{V}(\boldsymbol{x};d)$ and

$$\frac{\partial W_F}{\partial d} = \frac{\mathrm{d}}{\mathrm{d}d}\boldsymbol{F}(d) \cdot \boldsymbol{V}(\boldsymbol{x};d) + \boldsymbol{F}(d) \cdot \dot{\boldsymbol{V}}(\boldsymbol{x};d) = \frac{\mathrm{d}}{\mathrm{d}d}\boldsymbol{F}(d) \cdot \boldsymbol{V}(\boldsymbol{x};d)\ + W_F(\boldsymbol{U}(\boldsymbol{x};d), \dot{\boldsymbol{V}}(\boldsymbol{x};d)). \tag{3.8}$$

Since the topography and the velocity fields have sufficient smoothness, $\dot{\boldsymbol{V}}(\boldsymbol{x};d)$ belongs to the Hilbert space $H^1(B(d,t))$, which means $\dot{\boldsymbol{V}}(\boldsymbol{x};d) \in U_{ad}$. Thus,

$$\int_{B(d,t)} \left(\mathscr{C}^{\alpha\beta\lambda\mu} e_{\alpha\beta}(\boldsymbol{U}(\boldsymbol{x};d)) e_{\lambda\mu}(\dot{\boldsymbol{V}}(\boldsymbol{x};d)) + \mathscr{D}^{\alpha\lambda} e_{\alpha 3}(\boldsymbol{U}(\boldsymbol{x};d)) e_{\lambda 3}(\dot{\boldsymbol{V}}(\boldsymbol{x};d)) \right)\mathrm{dV} = \int_{B(d,t)} (\boldsymbol{F}(d) \cdot \dot{\boldsymbol{V}}(\boldsymbol{x};d))\mathrm{dV} \tag{3.9}$$

i.e.,

$$\int_{B(d,t)} W_C(\boldsymbol{U}(\boldsymbol{x};d), \dot{\boldsymbol{V}}(\boldsymbol{x};d))\mathrm{dV} = \int_{B(d,t)} W_F(\boldsymbol{U}(\boldsymbol{x};d), \dot{\boldsymbol{V}}(\boldsymbol{x};d))\mathrm{dV}. \tag{3.10}$$

Noting that

$$\frac{\mathrm{D}}{\mathrm{D}d} I(W_C) = \frac{\mathrm{D}}{\mathrm{D}d} I(W_F). \tag{3.11}$$

Substituting Eq. (3.6-3.8) into Eq. (3.11) and utilizing Eq. (3.10) yields

$$\int_{B(d,t)} W_C(\dot{\boldsymbol{U}}(\boldsymbol{x};d), \boldsymbol{V}(\boldsymbol{x};d))\mathrm{dV} + \int_{\partial B(d,t)} W_C V_n \mathrm{dS} = \int_{B(d,t)} \frac{\mathrm{d}}{\mathrm{d}d}\boldsymbol{F}(d) \cdot \boldsymbol{V}(\boldsymbol{x};d)\mathrm{dV} + \int_{\partial B(d,t)} W_F V_n \mathrm{dS}. \tag{3.12}$$

Since $\boldsymbol{U}(\boldsymbol{x},d) = \boldsymbol{V}(\boldsymbol{x},d)$ in the concerned compliance minimization problem (Guo et al., 2014), the compliance function satisfies

$$C = \int_{B(d,t)} W_C(\boldsymbol{U}(\boldsymbol{x};d), \boldsymbol{U}(\boldsymbol{x};d))\mathrm{dV}. \tag{3.13}$$

By leveraging Eq. (3.6, 3.12-3.13), we can derive the expression for the material time derivative $\frac{\mathrm{D}C}{\mathrm{D}d}$ as follows

$$\frac{\mathrm{D}C}{\mathrm{D}d} = 2\int_{B(d,t)} W_C(\dot{\boldsymbol{U}}(\boldsymbol{x};d), \boldsymbol{U}(\boldsymbol{x};d))\mathrm{dV} + \int_{\partial B(d,t)} W_C V_n \mathrm{dS} = 2\int_{B(d,t)} \frac{\mathrm{d}}{\mathrm{d}d}\boldsymbol{F}(d) \cdot \boldsymbol{U}(\boldsymbol{x};d)\mathrm{dV} + \int_{\partial B(d,t)} (2W_F - W_C) V_n \mathrm{dS}. \tag{3.14}$$

We note that the calculation of $\dot{\boldsymbol{U}}$ is eliminated in Eq. (3.14). Additionally, the numerical implementation of the sensitivity analysis described above is realized through finite element discretization.

3.3. Calculation and derivative of the velocity field

Until now, the derivation of compliance sensitivity remains unresolved for variables $\partial B(d,t)$, and V_n ($V_n = \boldsymbol{v} \cdot \boldsymbol{N}$). We notice that the geometry quantity V_n is only calculated on $\partial B(d,t)$. Since $B(d,t) = S(d) \times [-\bar{t}/2, \bar{t}/2]$ (shown in Fig. 10(a)), we have

$$\partial B(d,t) = \cup_{i=1}^{3} \Gamma_i, \tag{3.15}$$

with

$$\begin{cases} \Gamma_1 = B(d,t)|_{t=\bar{t}/2}, \\ \Gamma_2 = B(d,t)|_{t=-\bar{t}/2}, \\ \Gamma_3 = \partial S(d) \times [-\bar{t}/2, \bar{t}/2], \end{cases} \tag{3.16}$$

as shown in Fig. 10(b). For each point $\boldsymbol{x}' = \boldsymbol{x}'(\boldsymbol{x}; d)$ on the middle surface $S(d)$, the position is obtained by the perturbation operation from the point $\boldsymbol{x}$ of the original surface S_0, i.e.,

$$\boldsymbol{x}'(\boldsymbol{x}; d) = \boldsymbol{x} + h_S(\boldsymbol{x}; d) \cdot \boldsymbol{N}(\boldsymbol{x}, S_0), \tag{3.17}$$

where $\boldsymbol{N}(\boldsymbol{x}, S_0)$ is the positive normal vector of the surface S_0 taken at the point $\boldsymbol{x}$. Projecting the point $\boldsymbol{x}'$ to the upper surface Γ_1 and the lower surface Γ_2 along the local normal vector (shown in Fig. 10(c)), the corresponding projection points (after surface perturbation) are expressed as

$$\begin{cases} \boldsymbol{x}_1' = \boldsymbol{x}' + \dfrac{\bar{t}}{2}\boldsymbol{N}(\boldsymbol{x}', S(d)), \\ \boldsymbol{x}_2' = \boldsymbol{x}' - \dfrac{\bar{t}}{2}\boldsymbol{N}(\boldsymbol{x}', S(d)), \end{cases} \tag{3.18}$$

where $\boldsymbol{N}(\boldsymbol{x}', S(d))$ represents the positive normal vector of the surface $S(d)$ taken at the point $\boldsymbol{x}'$. Below, we take the upper boundary Γ_1 as an example and derive the velocity field induced by the instant change of parameter d. Substituting Eq. (3.17) into Eq. (3.18), we get

$$\boldsymbol{x}_1'(\boldsymbol{x}; d) = \boldsymbol{x}_0 + h_S(\boldsymbol{x}; d) \cdot \boldsymbol{N}(\boldsymbol{x}, S_0) + \frac{\bar{t}}{2}\boldsymbol{N}(\boldsymbol{x}', S(d)). \tag{3.19}$$

The velocity field $\boldsymbol{v}_1$ of Γ_1 is defined as the material time derivative of $\boldsymbol{x}'$ with respect to d, i.e.,

$$\boldsymbol{v}_1 = \frac{\mathrm{D}}{\mathrm{D}d}\boldsymbol{x}_1'(\boldsymbol{x}; d) = \frac{\partial}{\partial d}h_S(\boldsymbol{x}; d) \cdot \boldsymbol{N}(\boldsymbol{x}, S_0) + \frac{\bar{t}}{2}\frac{\partial \boldsymbol{N}(\boldsymbol{x}', S(d))}{\partial d}, \tag{3.20}$$

and we have

$$V_n^1 = \boldsymbol{v}_1 \cdot \boldsymbol{N}(\boldsymbol{x}_1', \Gamma_1), \tag{3.21}$$

where $\boldsymbol{N}(\boldsymbol{x}_1', \Gamma_1)$ is the outer normal vector of the boundary Γ_1 taking at the point $\boldsymbol{x}_1'$. The derivation of the velocity field of boundary Γ_2 is similar to the derivation above. In addition, due to the slenderness property of the structure, the integrals over the boundary Γ_3 are omitted. Considering that the topography field is defined through the surface-cutting operation and the multi-patch stitching scheme, the derivative of $h_S(\boldsymbol{x}; d)$ with respect to d reads

$$\frac{\partial}{\partial d}h_S(\boldsymbol{x}; d) = \frac{\partial h_S}{\partial h_{S_i}^{\mathrm{s}}}\frac{\partial h_{S_i}^{\mathrm{s}}}{\partial h_{S_i}}\frac{\partial h_{S_i}}{\partial h_{S_i^*}}\frac{\partial h_{S_i^*}}{\partial d}, \tag{3.22}$$

where h_{S_i} represents the topography field defined on the i-th surface patch S_i, the symbol $h_{S_i}^{\mathrm{s}}$ represents the extended definition via Eq. (2.18), and S_i^* is the intermediate surface (obtained from the surface-cutting operation) corresponding to the surface S_i. Here, $h_{S_i^*}$ is obtained via $h_{S_i^*}(\boldsymbol{x}; d) = h_{M^i}(\boldsymbol{p}; d)$ with $f_i(\boldsymbol{x}_0) = \boldsymbol{p}: \ S_i^* \to M^i$ denoting the i-th conformal mapping. The partial derivative of $h_{M^i}(\boldsymbol{p}; d)$ with respect to d is given by

$$\frac{\partial}{\partial d}h_{M^i}(\boldsymbol{p}; d) = \frac{\partial h_{M^i}(\boldsymbol{p}; d)}{\partial h_{i,k}(\boldsymbol{p}; d)}\frac{\partial h_{i,k}(\boldsymbol{p}; d)}{\partial d}, \tag{3.23}$$

where $h_{i,k}(\boldsymbol{p}; d)$ is the topography field function defined on the i-th domain by the k-th component, i.e., Eq. (2.7-2.16).

4. Solution techniques and implementation details

4.1. Solution techniques and the calculation of discrete sensitivity

In the current study, the shell FEM is performed in the commercial software Abaqus using the general-purpose S3 shell element, which provides precise solutions to structural responses for both thick and thin shells. The exploited triangulated unstructured meshes also reduce the difficulty in describing complex shell structures. In addition, the number of integration points along the thickness direction is chosen as $n_p = 7$, and the thickness integration rule is the Simpson formula.

Regarding Eq. (3.14), the corresponding discrete sensitivity is calculated via the finite element discretization. Let $S_\Delta(d) = \cup_{e=1}^{n_e} S_\Delta^e(d)$ be the triangulated mesh of the surface $S(d)$ with $S_\Delta^e(d)$ denoting the e-th shell element. The discrete bulk domain is expressed as $B_\Delta(d, t) = \cup_{e=1}^{n_e} B_\Delta^e(d, t) = \cup_{e=1}^{n_e} S_\Delta^e(d) \times [-\bar{t}/2, \bar{t}/2]$ with $B_\Delta^e(d, t)$ denoting the corresponding solid domain of the e-th shell element. At the implementation level, Eq. (3.14) is discretized as

$$\frac{\mathrm{DC}}{\mathrm{D}d} = 2\sum_{e=1}^{n_e}\left(\frac{\mathrm{d}}{\mathrm{d}d}\boldsymbol{F}(d)\cdot\boldsymbol{U}(\boldsymbol{x};d)\right)_e V_e + \sum_{e=1}^{n_e}\left(((2W_F - W_C)V_n)_e^{\text{upper}} + ((2W_F - W_C)V_n)_e^{\text{lower}}\right)A_e, \tag{4.1}$$

where symbols $(\cdot)_e$, $(\cdot)_e^{\text{upper}}$, and $(\cdot)_e^{\text{lower}}$ represent the values of $(\cdot)$ taking at $B_\Delta^e(d,t)$, $B_\Delta^e(d,\bar{t}/2)$, and $B_\Delta^e(d,-\bar{t}/2)$, respectively (as shown in Fig. 10(d)). In Eq. (4.1), V_e is the volume of the solid domain B_Δ^e, and A_e represents the area of the triangle S_Δ^e. In addition, the Heaviside function we utilized in this study is expressed as

$$\mathrm{H}_{\alpha,\epsilon}(x) = \begin{cases} 1, & \text{if } x > \epsilon, \\ \dfrac{3}{4}\left(\dfrac{x}{\epsilon} - \dfrac{x^3}{3\epsilon^3}\right) + \dfrac{1+\epsilon}{2}, & \text{if } |x| \le \epsilon, \\ 0, & \text{otherwise}, \end{cases} \tag{4.2}$$

where $\epsilon = 0.6$ is the width of numerical approximation. In order to avoid the interrupt height variation at the point $x = 0$, the specific Heaviside function H^* is obtained by the horizontal movement, i.e., $\mathrm{H}^*(x) = \mathrm{H}_{\alpha,\epsilon}(x-\epsilon)$. We exploit the following K-S function (Kreisselmeier and Steinhauser, 1980) to approximate the assembly operator (i.e., Eq. (2.8), Eq. (2.17), and Eq. (2.19)):

$$\chi = \max(\chi^1,\ldots,\chi^n) \approx \frac{\ln\left(\sum_{i=1}^n \exp(l\chi^i)\right)}{l}, \tag{4.3}$$

where l is a large positive number ($l = 100$ in the current study).

4.2. Design processes and technical remarks

The design processes for the topography of shell structures are summarized as follows, comprising three major modules: surface preprocessing, explicit topography description, and optimization iterations. Initially, the surface mesh is divided into patches based on geometric features. The intermediate surface is obtained through the surface-cutting operation for each mesh patch, and conformal mapping is performed using the CCM technique. The topography field function for each patch is then constructed using Eqs. (2.6-2.16). Moreover, the global topography field function is assembled using Eqs. (2.17-2.19). The middle surface and the shell structure are altered through Eq. (2.5), followed by the FEA process to obtain structural responses and sensitivities of the modified shell structure. The design variables are updated using the MMA (method of moving asymptotes) optimizer (Svanberg, 1987). This step, along with constructing the topography field function, altering the shell structure, and calculating responses and sensitivities, iterates until the convergence requirements are satisfied. The following technical comments further explain the details of the solution for this work.

Remark 1. In some shell theories, **the degenerated energy** (i.e., the integral of the density of strain energy over the middle surface S rather than the bulk B) is utilized to approximate the deformation behaviors, which will induce complicated surface variational problems in sensitivity analysis and extra computational burden (e.g., the discrete mean curvature of the surface). Fortunately, the shell element in this study and the equipped theory are constructed upon the bulk domain, naturally solving the above issues.

Remark 2. Although the TDF function is also utilized in the current work, the main framework and the central motivation are different from conventional topology optimization. Notably, the classical **volume fraction constraint** is not necessary for obtaining a well-posed optimization problem formulation.

Remark 3. Numerous methods exist for mapping a complex surface to a simpler domain in a plane. However, the CCM technique used in this study is based on discrete meshes, which can be integrated with existing CAE software and 3D scanning techniques. Moreover, the CCM technique preserves angles, ensuring the mesh quality of the plane parameter domain and reducing distortion in topography description caused by the mapping process.

5. Numerical examples

In this section, we first validate the effect of topography variations on improving the mechanical performance of shell structures. Next, representative examples are provided to verify the effectiveness of the proposed algorithm. Finally, factors that have dominant effects on the final design are investigated in detail. Unless otherwise stated, the geometry sizes and material properties are set as dimensionless. The material is isotropic and linearly elastic, with Young's modulus and Poisson's ratio chosen as $E = 1$ and ν=0.3, respectively. The objective of the optimization problem is to minimize the structural compliance (Eq. 3.1(b)), i.e., maximizing the structural stiffness. The optimization process terminates at the 300th step. The number of the shape control coefficients for every component is taken as 9 ($nr = 8$), and the knot vector is chosen as the common uniform form, i.e., $\Xi = \left\{-\pi,-\pi,-\pi,-\pi+1*\frac{2\pi}{7},-\pi+2*\frac{2\pi}{7},\ldots,-\pi+6*\frac{2\pi}{7},\pi,\pi,\pi\right\}$.

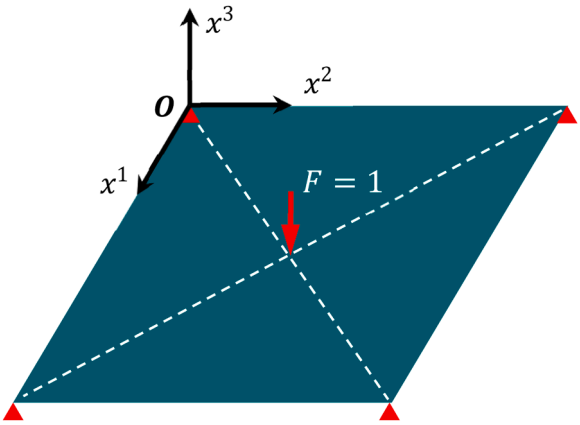

Fig. 11. Boundary conditions of the square plate example. The length of the side is 80, and the thickness of the plate is 0.2. The concentrated force with unit magnitude is loaded at the center.

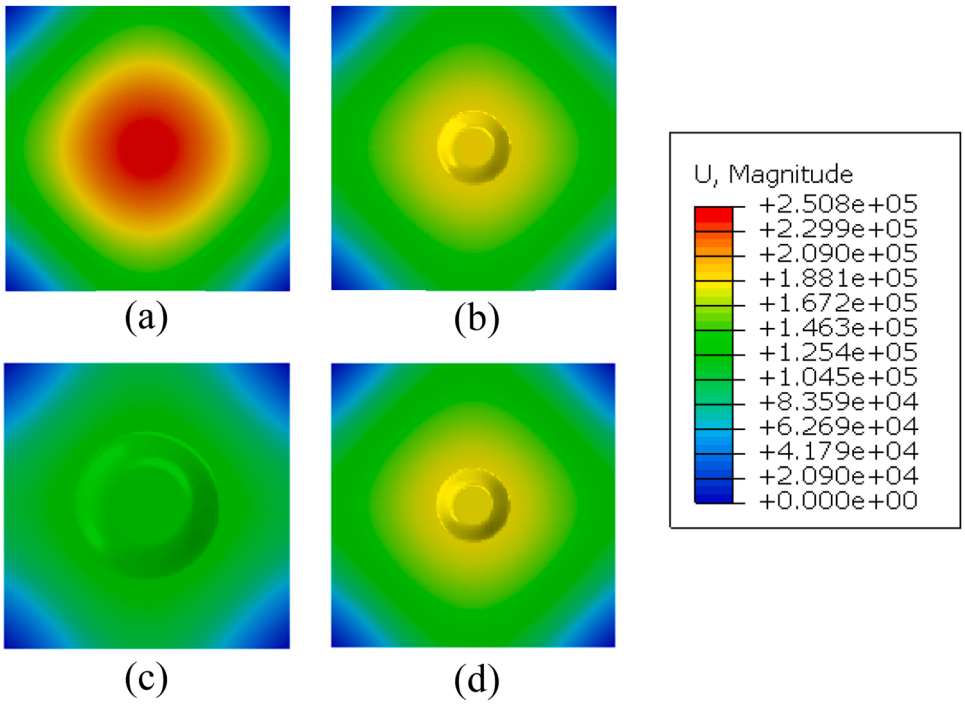

Fig. 12. Comparison between the displacement magnitudes of different topography settings. (a) Non-topography design with the maximum displacement magnitude $U^{mag}_{\max} = 2.51\text{e}5$. (b) Single topography component design with all shape coefficients set to 8. The height of the component is set to 4, and the maximum displacement reaches $U^{mag}_{\max} = 1.88\text{e}5$. (c) By increasing the shape coefficients to 16 while keeping the height at 4, the maximum displacement is changed to $U^{mag}_{\max} = 1.22\text{e}5$. (d) By increasing the height to 8 while keeping the shape coefficients at 4, the maximum displacement is changed to $U^{mag}_{\max} = 1.87\text{e}5$.

5.1. Mechanism validation

In order to eliminate the influence of the mapping process and the curved geometry of the original shell structure, a simple square plate subjected to a concentrated force is adopted here as the fundamental example. As illustrated in Fig. 11, the length of the side and the thickness are set to 80 and 0.2, respectively. To validate the function of the topography field, various parameters are set to produce diverse designs, as shown in Fig. 12.

Compared with the flat-topography design in Fig. 12(a), the protrusive circular truncated cones in Fig. 12(b-d) significantly decrease the displacement magnitude and improve structural performances. We can observe that the performance of the magnified topography (Fig. 12(c)) is better than the basic topography (Fig. 12(b)). A natural conclusion is that the larger the topography, the

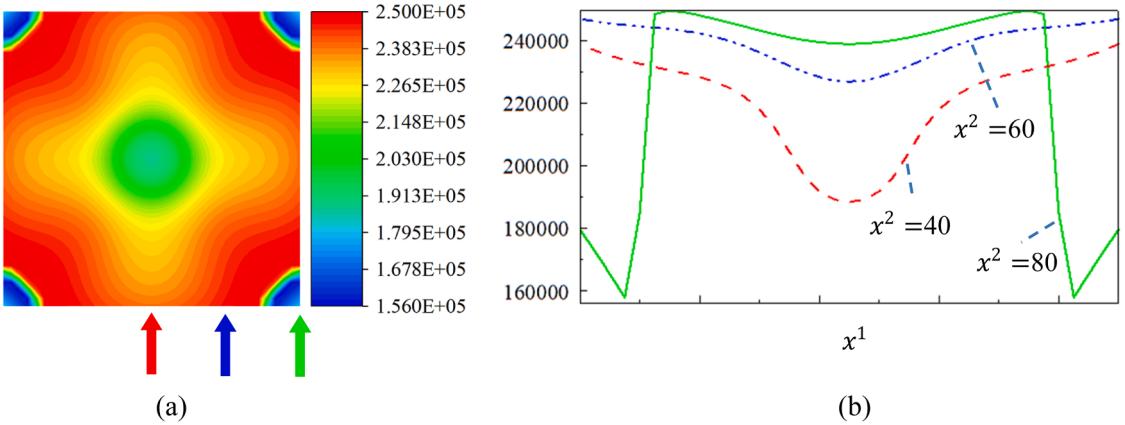

Fig. 13. Effect of the location of the basic topography component. (a) Cloud map that describes the variation of the displacement magnitude at the loading point as the basic topography component moves. (b) Three curves that characterize the low-dimensional distribution of the cloud map (a) along the red, blue, and green arrows, respectively.

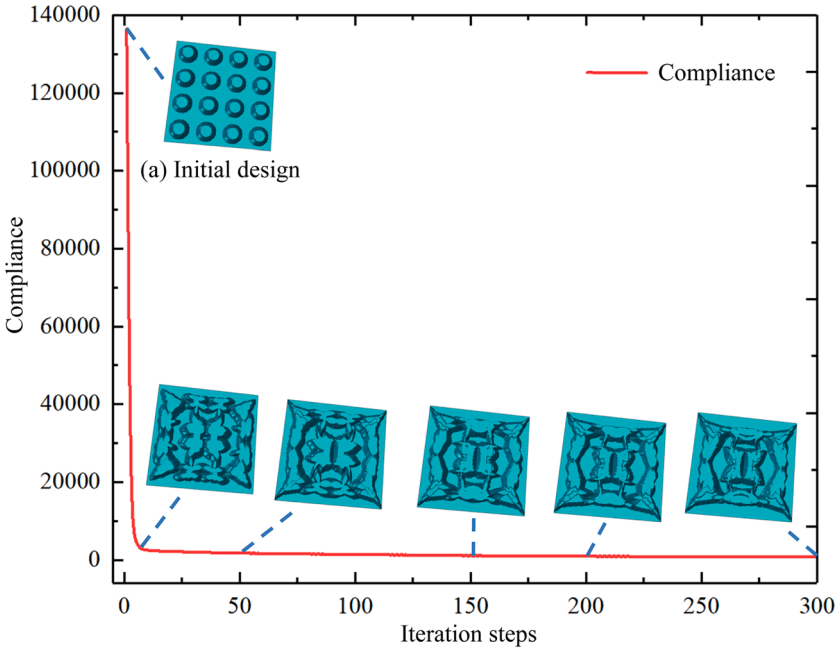

Fig. 14. Iteration histories and intermediate results of the basic topography design problem of the plate structure. (a) Initial design. According to the iteration sequence, the displayed structures represent intermediate structures of the 1st step ($C = 136{,}443.80$), the 5th step ($C = 4868.34$), the 50th step ($C = 1768.73$), the 150th step ($C = 1145.91$), the 200th step ($C = 959.54$), and the 300th step ($C = 876.03$). The value of the compliance function of the original structure (Fig. 11) is = 2.51e5.

better the structural performance. Unfortunately, this opinion does not hold. Assuming the basic topography is continuously enlarged until its central even region covers the whole plate, the resultant structure will regress to the flat topography design and obtain a worse structure response. This phenomenon is also the core reason the volume fraction constraint is not required in the topography optimization.

We further explored the effect of topography location, i.e., the distribution of the function $U_{\max} = U_{\max}(x^1, x^2)$, where $U_{\max}$ is the x^3-direction displacement of the loading point (in this case, the magnitude of $U_{\max}$ is twice the compliance). (x^1, x^2) is the in-plane coordinate of the central point of the basic topography design (Fig. 12(b)). By altering the coordinates of the central point of the basic topography design, we can obtain a series of displacements, and the function distribution is illustrated in Fig. 13(a). Each point in this cloud map is assigned a specific value, representing the magnitude of the function $U_{\max}$ when the basic topography is located at this position. From the figure, we can observe the non-convexity of the optimization problem (the objective function is a non-convex function about the topography coordinate), which also verifies the necessity of constructing an algorithm to design the shell

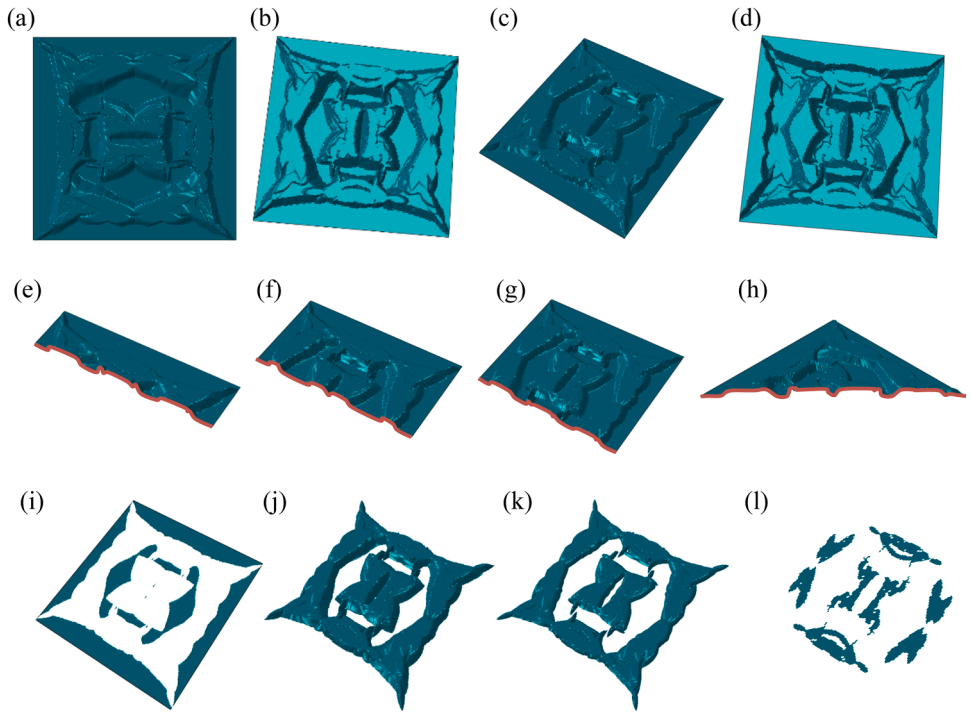

Fig. 15. Different views of the final design. (a) Front view 1. (b) Front view 2. (c) Front view 3. (d) Back view 1. (e-g) Cross-section diagrams at the transverse quarter position, at the transverse half position, and the three-quarters position. (h) Cross-section diagram along the diagonal direction. (i-l) Height filter diagrams of the zone of the initial height, the perturbed zone, the zone where the height is larger than half of the maximum height prescribed, and the zone where the height is at the maximum value.

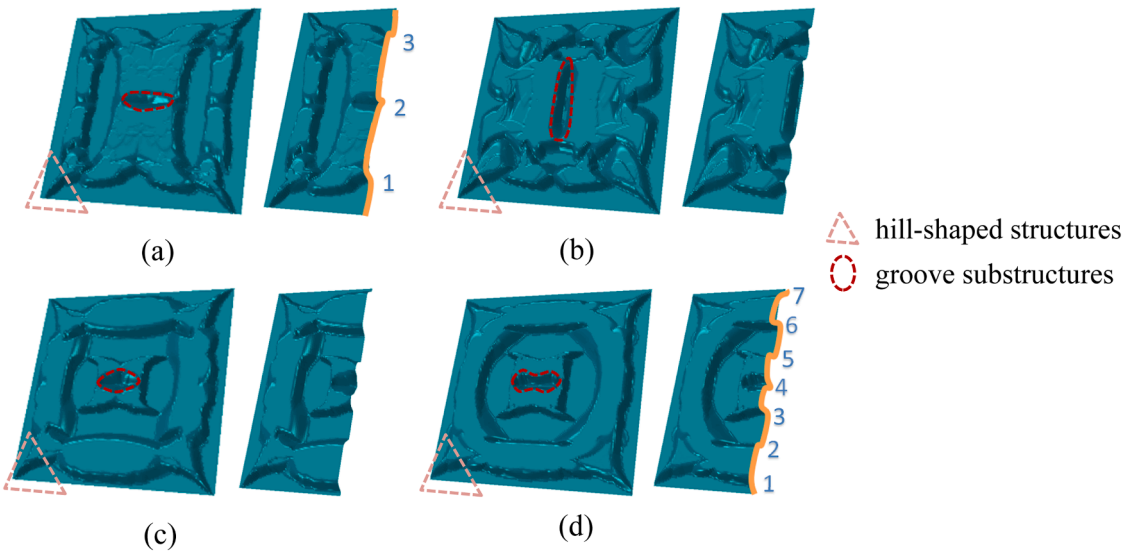

Fig. 16. Final designs of different thickness settings. (a-d) The thicknesses are 0.05, 0.1, 0.4, and 0.8, respectively. The compliance functions of these final designs are 2.20e4, 2.24e3, 312.66, and 262.56, respectively. The corresponding initial layouts of components for these six examples are set the same as Fig. 14(a), and the related initial compliance functions are 7.21e6, 9.53e5, 17,182.94, and 2356.02, respectively. The reduction rates of the compliance functions (obtained from reduced displacement magnitude over the displacement magnitude of the initial design) are 99.69 %, 99.76 %, 98.18 %, and 88.86 %, respectively.

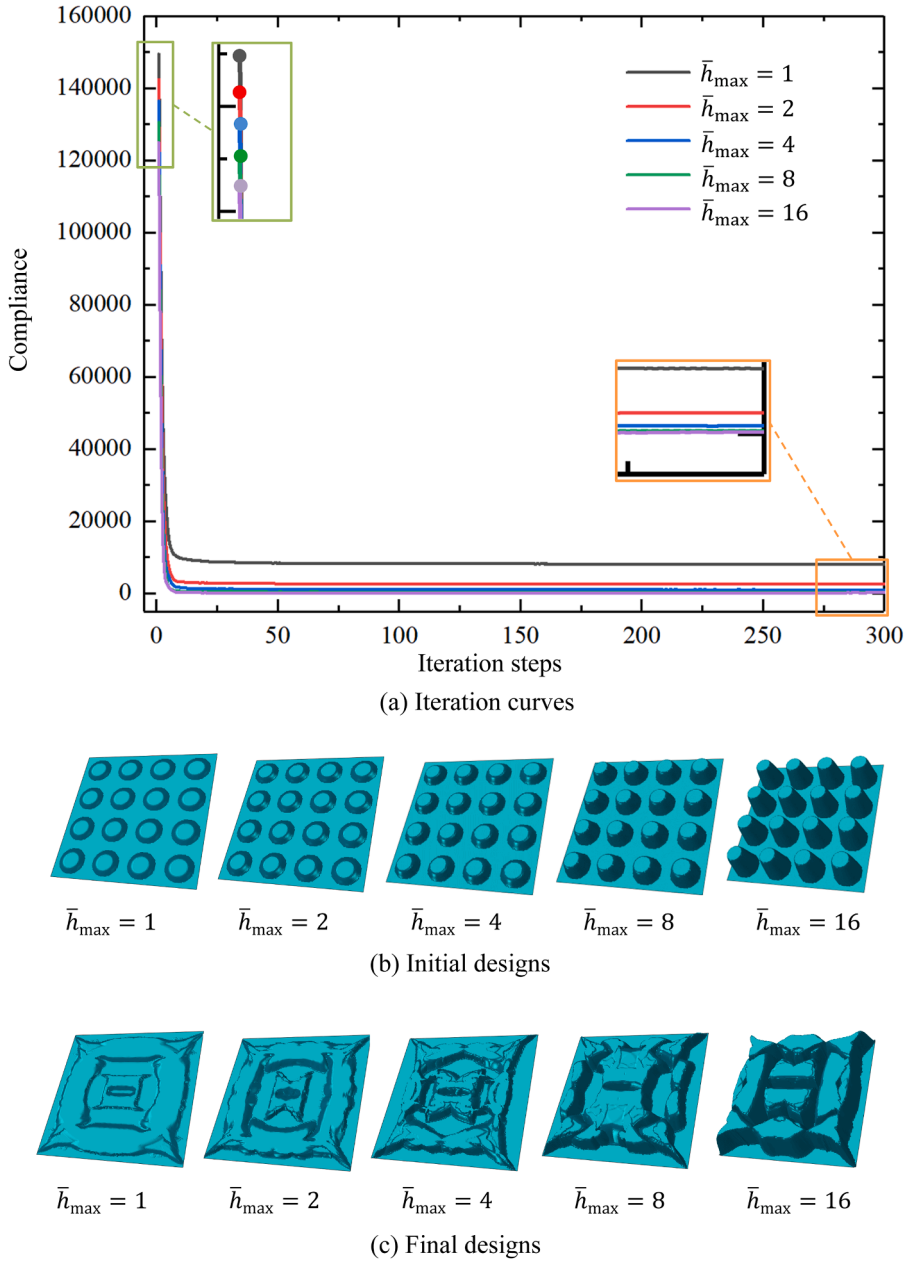

Fig. 17. Final designs of different height settings. (a) Iteration curves. (b) Initial designs corresponding to the cases of topography heights set as 1, 2, 4, 8, and 16, respectively. The compliances of the initial designs are 149,410.66, 142,453.00, 136,443.80, 130,516.98, and 124,903.23, respectively. (c) Final designs corresponding to the cases of maximum topography heights set as 1, 2, 4, 8, and 16, respectively. The compliances of the final designs are 8007.17, 2560.21, 876.03, 350.29, and 160.26, respectively.

topography. In addition, low-dimensional distribution features of the function along three arrows (in Fig. 13(a)) are shown in Fig. 13 (b), in which these three curves plot the function $U_{\max} = U_{\max}\left(x^1, \overline{x^2}\right)$ with the coordinate x^2 fixed at $x^2 = 40$ (red curve), $x^2 = 60$ (blue curve), and $x^2 = 80$ (green curve).

5.2. *Designing the topography of a plate structure*

In this section, we explore the effects of problem-setting parameters (i.e., the thickness of the plate, the boundary conditions, and the initial curvature of the geometry model) on the final design. Considering that the mapping process and the curved geometry may impede the observation of experiment phenomena, the plate example in Fig. 11 is utilized. First, we conduct a basic topography

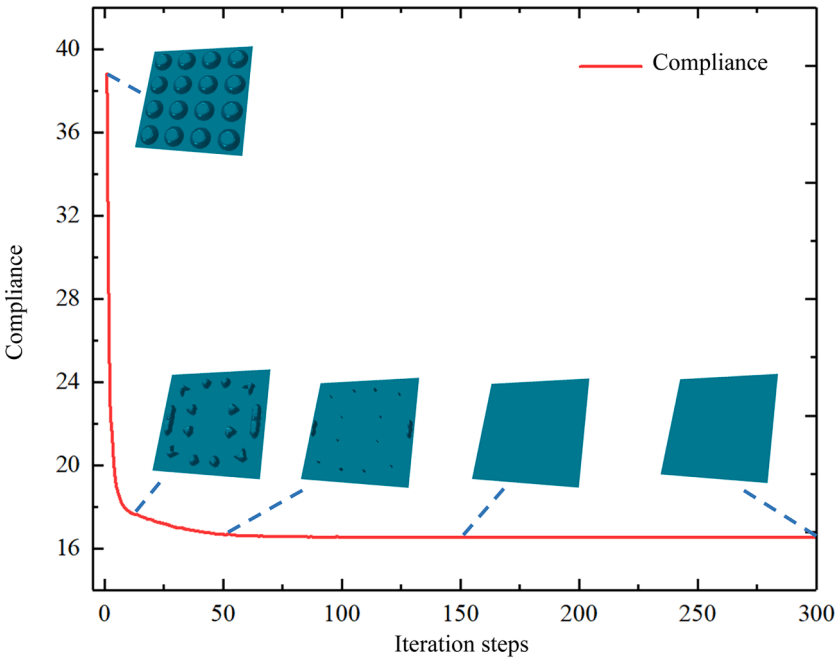

Fig. 18. Iteration histories and intermediate results of the topography design problem of the plate structure subjected to in-plane force.

optimization without changing any problem-setting parameters. The initial design with 4 × 4 components is set as Fig. 14(a). The initial topography heights and the maximum topography heights (i.e., $\overline{h}_i$ and $\overline{h}_i^{\max}$) are both set as 4. The entire iteration history is displayed in Fig. 14, from which we can observe that the topography is smooth throughout the optimization, and the compliance function decreases rapidly in the first 20 steps owing to the convergence advantage of the MMC framework. After the 20th step, the optimization progress gradually tends to the modification of the topography details. After the 50th step, the objective function converges to a stable value.

The final design is presented in Fig. 15, which achieves a displacement reduction of around 99.36 % (the compliance objective function decreased from 136,443.80 to 876.03). The significant promotion is mainly achieved by the corrugation configuration across the sections, as illustrated in Fig. 15(a-h). As seen from above, sharp hill-shaped structures are formed near the four fixed ends, and the cross sections contain multiple peaks and valleys. These features efficiently restrain the out-of-plane deformation induced by the support reaction. Diverse height filter diagrams are illustrated in Fig. 15(i-l), which prove the complexity of the topography description and the effectiveness of the related constructing framework.

Considering that the thickness factor significantly affects the magnitude difference between stiffnesses of the in-plane and out-of-plane directions, potentially influencing the proposed algorithm's effect, we set various thicknesses from 0.05 to 0.8 in the plate design example and keep other parameters the same. The final designs are presented in Fig. 16, which provides an overview of the effect of the thickness factor. Overall, the thinner the shell, the more the algorithm improves. As the thickness increases, the final-designed topography gradually diffuses from the center area to the surrounding area and forms a circle shape. The main reason is that the transverse bending and shearing stiffnesses rise as the thickness increases, which weakens the improving effect of uneven topography and drives the topography to form more ups and downs (e.g., three height changes in the section diagram in Fig. 16(a) versus seven height changes in the section diagram in Fig. 16(d)). Despite the differences in the final designs, some common structures form in the designed structures. For instance, sharp hill-shaped structures form near the four fixed ends. Interestingly, closer inspections of the designed structures show that the narrow and long groove substructures appear at the center points in all final structures, which proves the efficiency of improving the local stiffness at the loading point.

In addition, the height influences the effect of topography and the optimization results. Hence, we further explored the role of height in topography design. In the following five cases, we set the topography heights (including initial heights $\overline{h}_i$ and maximum heights $\overline{h}_i^{\max}$) as 1, 2, 4, 8, and 16, as shown in Fig. 17. Among them, when the height is set to 4, it is the design example in Fig. 14. Iteration curves of different settings are plotted in Fig. 17(a), from which we can find out that these curves start from different initial values, and undergo similar variation tendencies, and converge to respective final values. Comparing different iteration curves, we can find that both the compliances of the initial design and the final design decrease as the height increases. This indicates that the rise in topography height will improve the structural stiffness and the optimization effect of the final design. The initial designs are illustrated in Fig. 17(b). These topography components differ only in height. Indeed, with the increase in height, the compliance gradually decreases, and the structural stiffness gradually increases. Nevertheless, it is worth noting that the compliance decreases slowly despite the height increasing exponentially (i.e., the increment of material volume increases exponentially) in these initial design cases. This

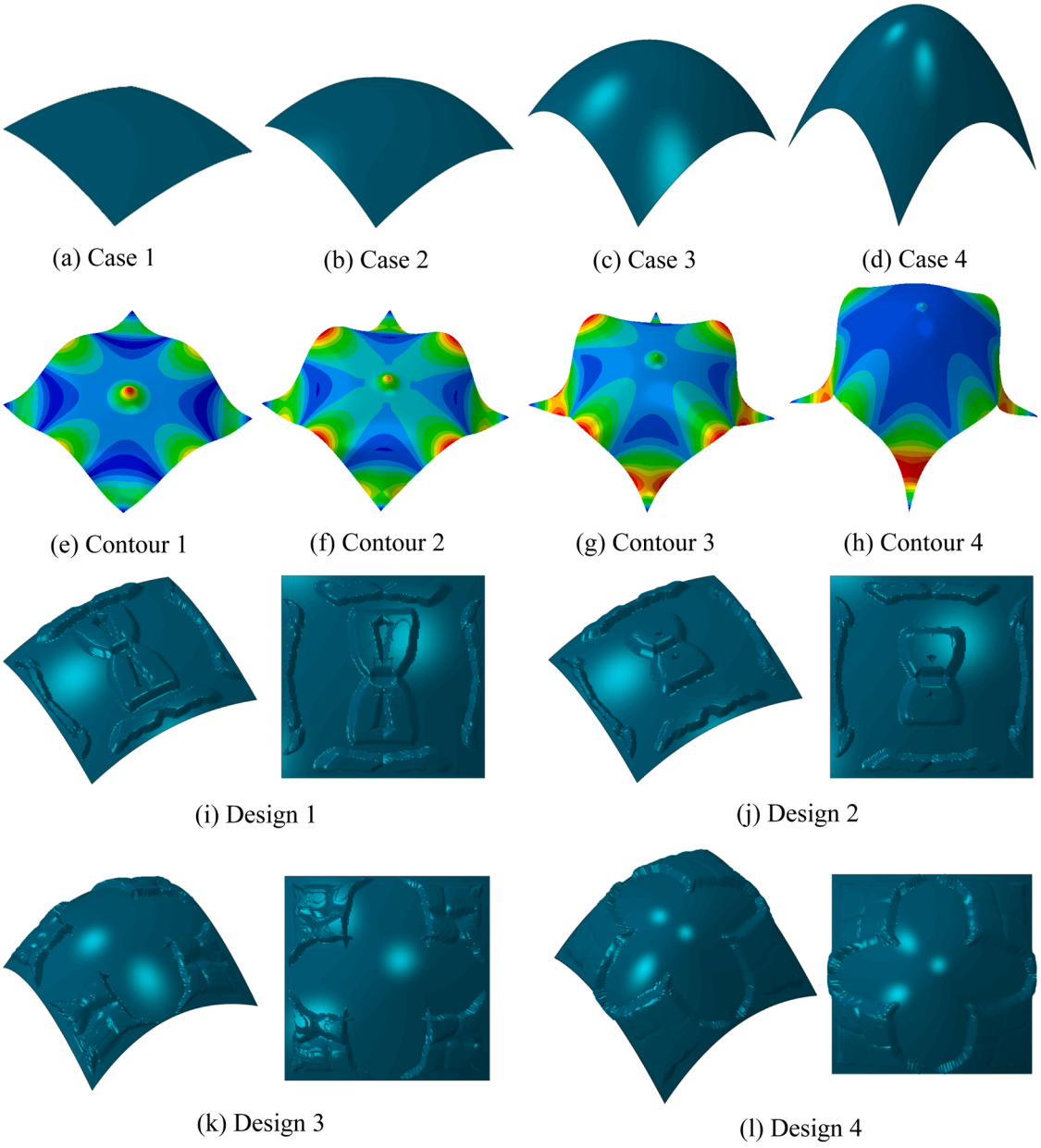

Fig. 19. Modified middle surfaces and the corresponding final designs. (a-d) The parameter γ of these cases are set as 10, 20, 40, and 80, respectively. (e-h) The contours (corresponding to cases 1–4) of displacement magnitude are plotted on the deformed shapes. The compliance functions of the non-topography designs of cases 1–4, i.e., (a-d), are 2095.38, 1351.56, 1119.50, and 1260.84, respectively. (i-l) The final designs correspond to cases 1–4, and the compliance functions of the final designs are 156.36, 169.44, 426.60, and 216.72, respectively. The reduction rates of the compliance function are 92.54 %, 87.46 %, 61.89 %, and 82.82 %, respectively.

illustrates the necessity of rational and systematic design, i.e., materials cannot be sufficiently utilized if we directly employ the "empirical" initial designs. The validation of the former assertion is also provided in Fig. 17(c). Using topography optimization, the compliance of the final designs can decrease exponentially (the compliance decreases by 1/2~5/7 for every doubling of the topography maximum height). The height limitation variation also causes differences in the optimized structures. It is evident that with the elevation of the height, the initially connected whole topography gradually separated, forming several isolated islands. In addition, similar structural features still exist in different designs, i.e., groove substructures are formed at the loading points, and hill-shaped structures are formed at the four corner points (analogy to Fig. 16).

The effectiveness of topography design has been proved in previous examples. Nevertheless, does an uneven design always work better than a flat topography design? The answer is negative. Next, we provide an intuitive example to refute such an opinion and explore the influence of boundary conditions on the final design. The geometry and material of the current example are set the same as

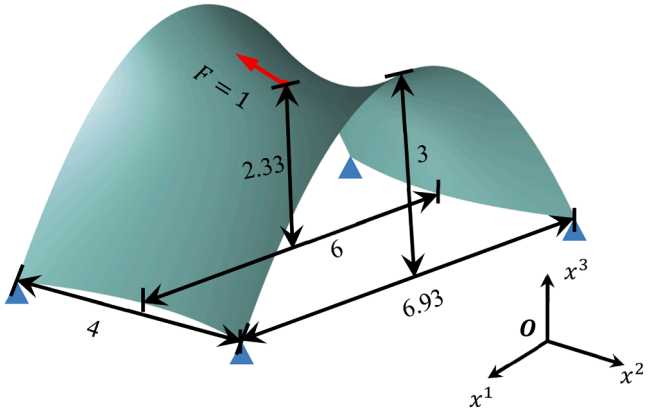

Fig. 20. Problem settings of the saddle-shaped shell example. The shell structure is fixed at four corners and subjected to a concentrated force at the saddle point. The force with a unit magnitude is applied along the $-x^2$ direction. The thickness is set as 0.02.

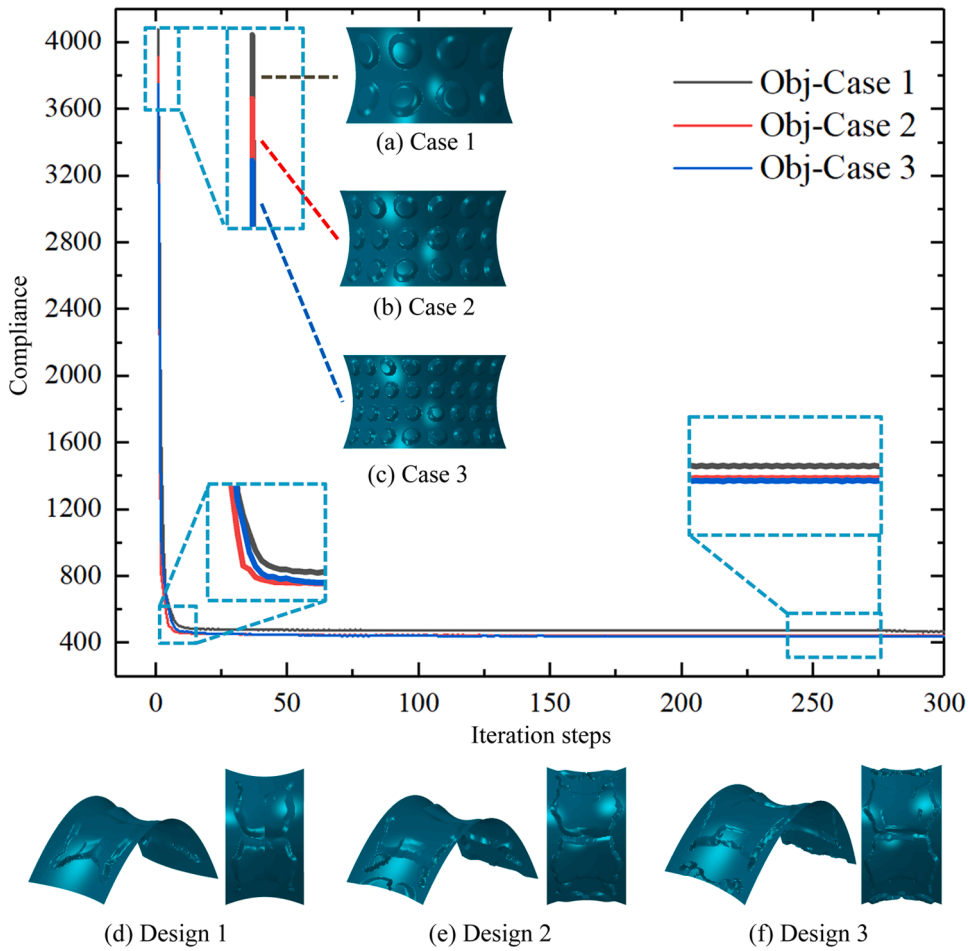

Fig. 21. Initial designs, iteration curves, and final designs of different component layouts. The compliance functions of the initial designs (a-c) are 4077.04, 3910.32, 3749.56, respectively. The compliance functions of the final designs (d-f) are 463.62, 444.84, 435.84, respectively.

in Fig. 11; the only difference is that the concentrated force is rotated to the x^2 direction, and the loading point is still the center of the plate. The initial design is the same as Fig. 14(a), and the iteration history is illustrated in Fig. 18. From the curve, we can still see that the optimization converges quickly, and the compliance function gradually decreases. Most striking is the structure evolution process, which illustrates that the protruding topography decreases and vanishes step by step. However, this phenomenon is consistent with the

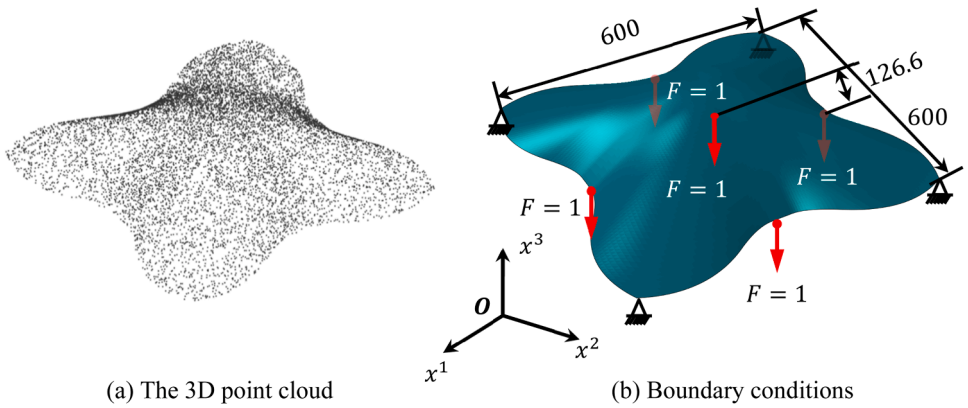

Fig. 22. Problem settings of the cone-shaped shell example. The geometry model is reconstructed from the 3D point cloud data (a). (b) The shell structure (the thickness is set as 3) is fixed at four corners and subjected to five concentrated forces (four at the middle of edges and one at the center of the surface). The forces are applied along the $-x^3$ direction.

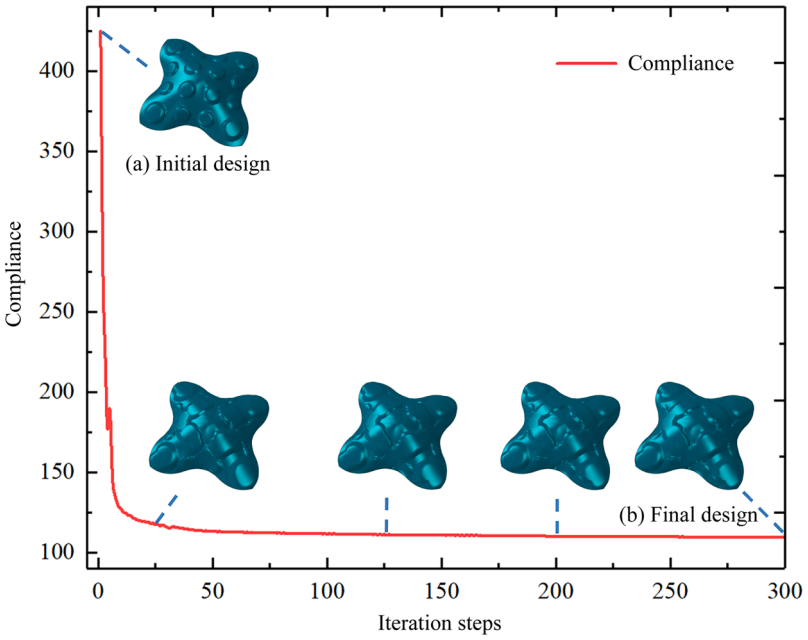

Fig. 23. Iteration histories and intermediate results of the cone-shaped shell example. (a) Initial design ($C = 424.74$). (b) Final design ($C = 109.42$).

basis of this study, that is, the external load is in-plane in this example, and the optimal topography should utilize the in-plane stiffness as much as possible, which drives the initial protruding components to vanish.

The effect of curvature on the mechanical performance of shell structures can be significant and is influenced by various factors, e.g., shells with higher curvature tend to be stiffer against certain types of loads (particularly those acting perpendicular to the shell's surface) (Lazarus et al., 2012), and curvatures may lead to better load-carrying mode (Bischoff et al., 2004). Hence, we further examined the influence of geometry curvature on the final design in this example. The middle surfaces (shown in Fig. 19(a-d)) are modified according to the following equation:

$$x^3 = \gamma * \frac{\left((x^1 - 40)^2 + (x^2 - 40)^2\right)}{3200}. \tag{5.1}$$

The boundary conditions, the thickness, and the material parameters remain the same as in the example of Fig. 11. The initial component layout is set the same as in Fig. 14(a). Fig. 19(i-l) presents the final designs of these examples. We note that in a proper range (Fig. 19(a-c)), the higher the curvature, the stiffer the original shell structure. For case 4, areas around four support ends are weak, with enormous displacement magnitude, as shown in Fig. 19(h). Hence, the overall stiffness of the structure in case 4 is less than that in case 3. The improvement of topography design decreases as the original structure becomes stiffer (in the order of Case 1, Case 2,

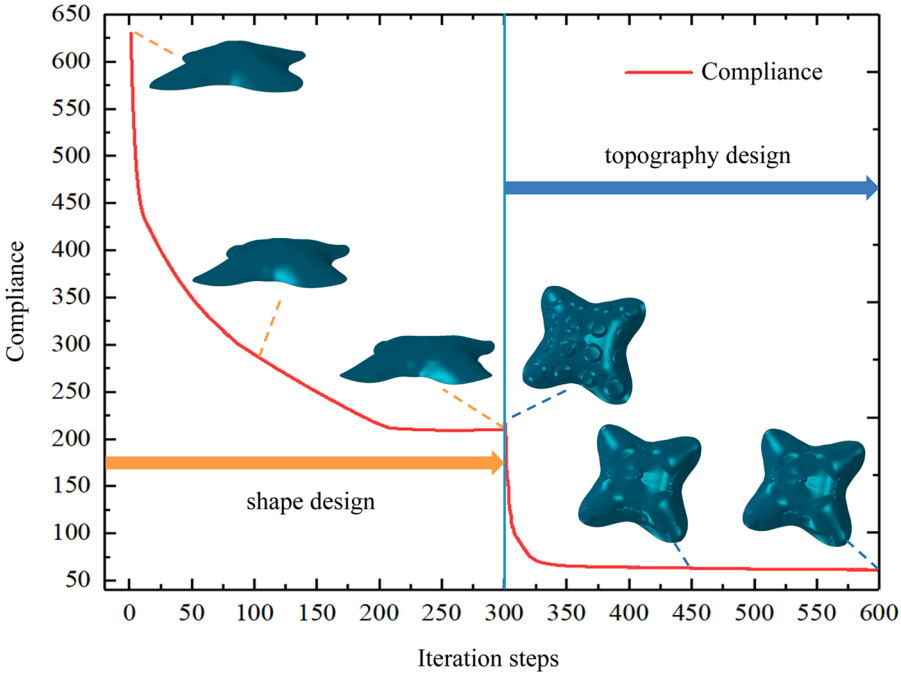

Fig. 24. Iteration histories and intermediate results of the shape-topography-joint design for the cone-shaped shell example. Before the 300th step, the iteration process utilizes the shape design approach to optimize the structural performance, in which the compliance function is reduced from 629.80 to 210.08. At the 301st step, the proposed topography design method is employed to improve the structure property further; the base surface is the resultant surface of the shape optimization process, and the compliance function is ulteriorly reduced to 61.62.

Case 4, and Case 3). For high curvature structures (Case 3 and Case 4), areas surrounding the central points are stiff enough, and the weak areas are around the four support points, which causes the topography components to disperse into corners to enhance the local stiffness.

5.3. Optimizing topography of surface shell structures via the CCM technique

The CCM technique is necessary to obtain the topography design for shell structures whose curvature varies spatially. This section provides two representative models to verify the algorithm's effectiveness in handling shell structures and validate the potential to construct joint optimization algorithms for ulterior performance improvement.

The saddle-shaped shell example

The first example is a saddle-shaped shell, whose geometry sizes and boundary conditions are illustrated in Fig. 20. The process of constructing the surface topography is straightforward, i.e., directly utilizing the CCM technique and the embedded topography description. Here, we examined the effect of the initial component layout on the final design. Fig. 21 (a-c) demonstrates three types of initial structures, where components are placed as 4×2, 6×3, and 8×4, respectively. The iteration curves are plotted in Fig. 21, from which we can observe that the overall trends are consistent, and all optimization processes converge to approximate values. The corresponding final topography designs are illustrated in Fig. 21(d-f). The final designs show that the topography distributions in central zones are similar, and narrow grooves are formed in all these models. Additionally, as the number of components increases, more structure details occur in the edge areas to further improve the structure performance.

The cone-shaped shell example

For the second example, we utilize the cone-shaped shell reconstructed from a 3D point cloud (obtained by the 3D scanning technique) to verify the potential for joint optimization with existing shape optimization methods. The geometry sizes and the boundary conditions are presented in Fig. 22. First, we conduct the proposed topography design approach. The iteration histories and intermediate results are shown in Fig. 23, in which we can observe that the optimization and the designed structure converge quickly. Four corners of the final design bulge to improve the local stiffness near the support points. Then, we conduct the shape-topography-joint design, as presented in Fig. 24. As can be seen from the curve, the topography optimization further improves the shape optimization results. The result of the experiment indicates that the joint optimization can obtain a stiffener structure than designing the shell's shape (the 300th structure in Fig. 24) or topography (Fig. 23(b)) independently. In addition, there are significant differences between the results of the joint optimization and the independent topography design, which shows the sensitivity of the topography design to the base surface.

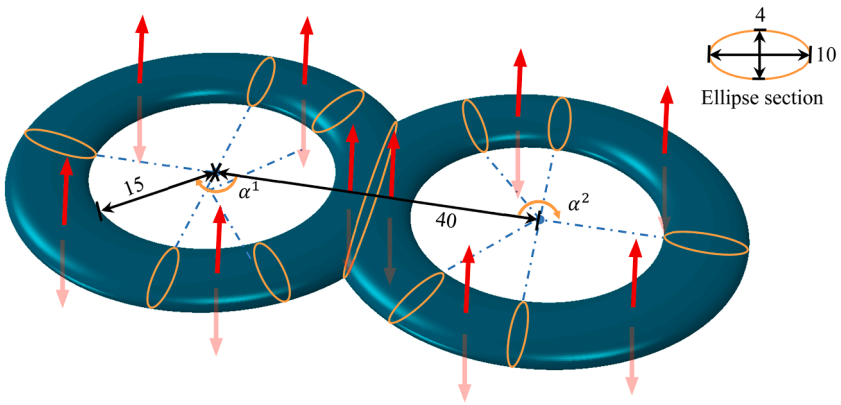

Fig. 25. Problem settings of the eight-shaped torus example. The orange circles are fixed boundary conditions distributed along the circular direction, and the circular coordinates (i.e., α^1 and α^2) are $\frac{\pi}{4}$, $\frac{\pi}{2}$, π, $\frac{3\pi}{2}$, $\frac{7\pi}{4}$. The red arrows are concentrated forces applied perpendicular to the surface. The circular coordinates of these forces are 0, $\frac{3\pi}{8}$, $\frac{3\pi}{4}$, $\frac{5\pi}{4}$, $\frac{15\pi}{8}$, and the radial distances between the applied points to the circle center are all set as 20. The thickness in this example is 0.01. In this example, the elastic modulus is set as 210,000, and the magnitude of forces is set as 100.

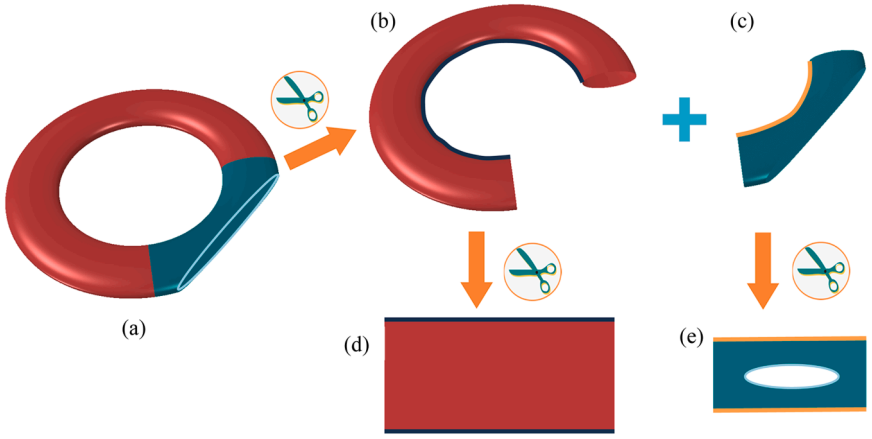

Fig. 26. Geometry preprocessing of the eight-shaped torus surface (taking the left half as the example). (a) The half model is a torus surface that has an open boundary. (b-c) Here, we divide the original surface into two independent patches according to the geometry feature. (d-e) Each patch is mapped to a plane rectangle domain after the surface-cutting operation. Note that the boundary of the original surface is mapped to a plane hole in (e).

5.4. Designing topography for complex shell structures

In the current subsection, we leverage two complex shell structures to demonstrate the importance of the surface-cutting operation and the multi-patch stitching scheme.

The eight-shaped torus shell example

The first eight-shaped torus shell structure is shown in Fig. 25. Apparently, this model cannot be directly mapped to a plane rectangle. Hence, the additional operations are leveraged to construct the surface topography, as shown in Fig. 26. The initial components are placed as Fig. 27(a) and the intermediate designs are demonstrated in Fig. 27. As can be seen, the optimized structure at the 150th step is close to the final design and the final compliance function is reduced to 9.09 % of that of the initial layout.

The vase example

For the following vase example shown in Fig. 28, additional preprocessing is not necessary from the perspective of algorithm implementation; that is, the mapping technique can be directly applied to the middle surface. However, as displayed in Fig. 28(c), the direct-mapping strategy induces unavoidable global distortions to the component layout. Hence, the multi-patch stitching scheme is leveraged to divide the whole surface into two parts, i.e., the to-be-designed body patch and the undesigned bottom patch, and the initial component is placed as presented in Fig. 28(d), from which we can observe that the topography distortion problem is well addressed. The iteration history and the final design are demonstrated in Fig. 29. As the optimization advances, the topography components gradually move towards the bottleneck to increase the radius here and reduce the local curvature. On the other hand, the bottom area gradually forms four circularly distributed bars, which enhances the local stiffness near the fixed ends. At last, the final

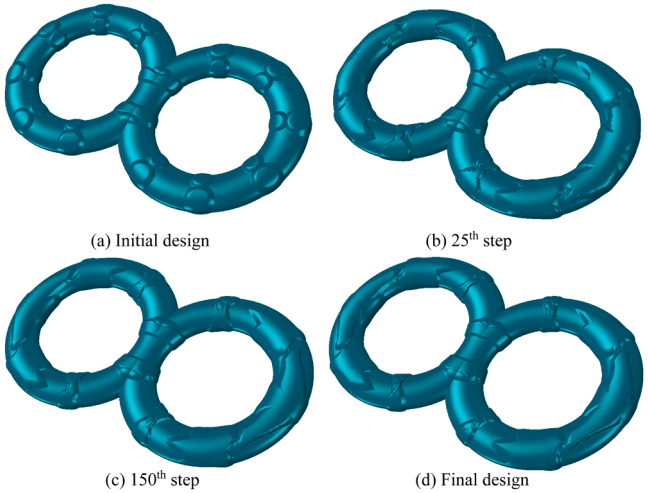

Fig. 27. Iteration histories, intermediate results, and the final design (300th step) of the eight-shaped torus shell example. (a) Initial design (C = 31,631.04). (b) The design of the 25th step (C = 5110.71). (c) The design of the 150th step (C = 3458.74). (d) The final design (C = 2876.67).

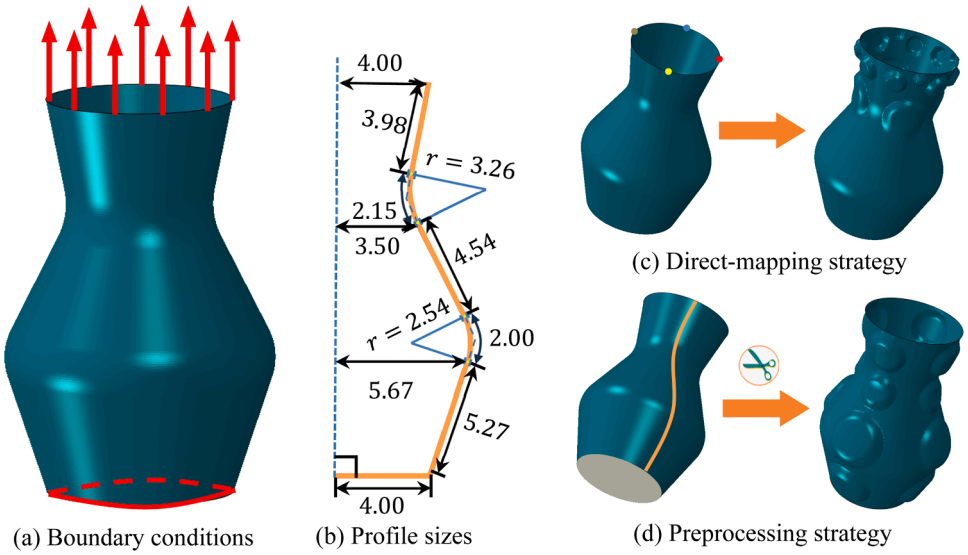

Fig. 28. Problem settings of the vase example (the thickness is 0.05). (a) The bottom of the vase is clamped, and the edge is subjected to a linear load of unit magnitude in a vertical direction. (b) The geometry model is generated by rotating the profile around the central axis. (c) The direct-mapping strategy results in massive distortions of component layout, which is intrinsic and unavoidable for the global mapping approach. (d) However, the distortion challenge can be resolved via the preprocessing strategy. Meanwhile, the undesigned domain (the grey bottom patch) is divided due to its zero-strain-energy state.

design reduces the compliance function by 78.98 % compared with the initial design.

6. Conclusions and extensions

In this article, we propose a novel and systematical structure optimization procedure for designing the topography distribution of complex shell structures by combining the MMC method and the CCM technique. The embedded description enables us to construct the topography variation on general surfaces and perfectly attaches the topography component to the base surface. The introduced TDF function and the enhanced spline component representation endow the proposed algorithm with the ability to describe complicated surface topography. By employing the surface-cutting operation and the multi-patch stitching scheme, the application scope of the proposed method is significantly enlarged, and the mapping distortion challenge is well addressed. Numerical examples demonstrate the capabilities of the proposed framework to enhance stiffness. Compared with existing methods, including the CAD-based and node-based shape optimization methods, the MMC-based model in this study offers a straightforward and easy-to-implement way to

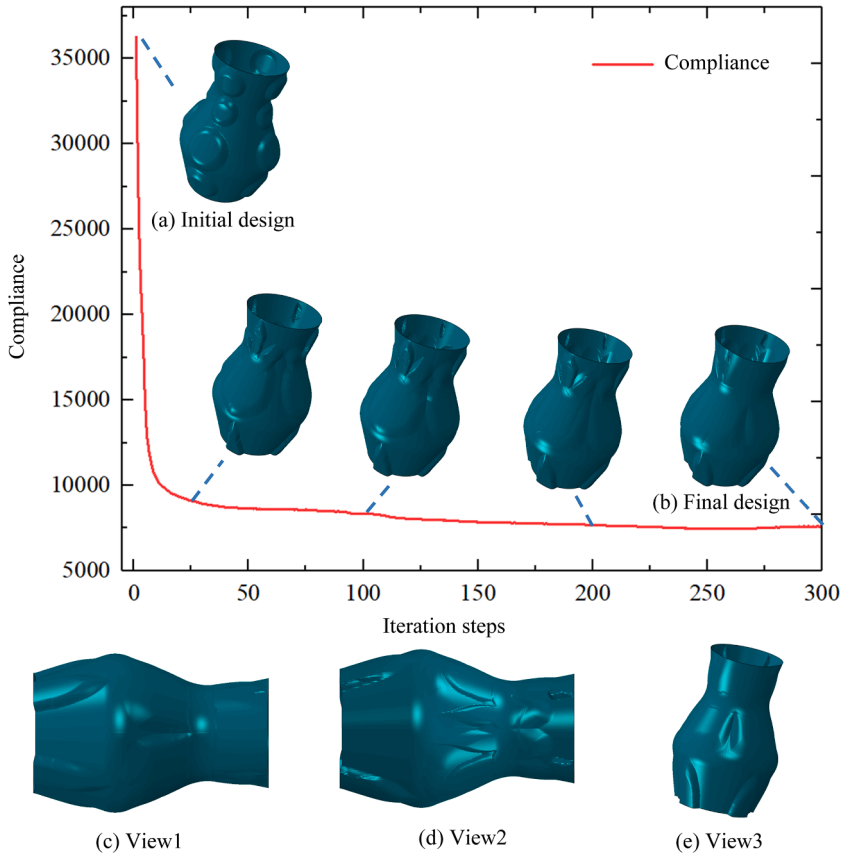

Fig. 29. Iteration histories, intermediate results, and the final design of the vase example. (a) Initial design (C = 36,268.51). (b) Final design (C = 7623.96). (c-e) Different views of the final design.

optimize complicated local topography since the parameterization process in CAD-based methods, and the filtering operations in node-based methods are eliminated. The proposed algorithm can achieve fast convergence with few iteration steps and design variables owing to the MMC method. Additionally, the explicit description endows the topography with mechanics, geometry, and engineering connotations (similar to ribs) and makes the final design more interpretable.

Nevertheless, as the first step towards explicit topography design, the present work has two major limitations. The structural response to be optimized is limited in the static compliance regime, and complex structural responses remain unexplored. In addition, although our approach has several advantages, such as few design variables, high computational efficiency, and good convergence, the integrated MMC method is a generalized dynamic ground structure approach with the shortcoming of initial dependence.

Consequently, this study can be expanded in multiple directions: (1) apply topography design to other mechanics problems, such as guiding the paths of cracks (Feng et al., 2023; Liu et al., 2023; Mitchell et al., 2017); (2) topography variation is essentially the altering of geometry domain, hence has the potential to improve other physics responses, e.g., thermal conduction and optics; (3) introduce the growth mechanism of components (Cui et al., 2022) to improve the design ability of the algorithm; (4) topography-designed shell structures are similar to sheet metal structure, therefore simultaneously optimizing structure topography and considering manufacturing methods (such as milling, welding, additive manufacturing, digital incremental forming, and mega-/giga-casting) is also a promising direction.

CRediT authorship contribution statement

Wendong Huo: Writing – original draft, Visualization, Validation, Software, Investigation, Formal analysis, Data curation, Conceptualization. **Chang Liu:** Writing – review & editing, Writing – original draft, Supervision, Resources, Project administration, Methodology, Investigation, Funding acquisition, Conceptualization. **Yilin Guo:** Writing – original draft, Investigation, Data curation. **Zongliang Du:** Writing – review & editing, Visualization. **Weisheng Zhang:** Writing – review & editing, Formal analysis. **Xu Guo:** Writing – review & editing, Supervision, Resources, Project administration, Methodology.

Declaration of competing interest

The authors declare that they have no known competing financial interests or personal relationships that could have appeared to influence the work reported in this paper.

Acknowledgment

This work is supported by the National Key R&D Program of China (2022YFB3303000), the National Natural Science Foundation (11821202, 12472344) and 111 Project (B14013).

Data availability

Data will be made available on request.

References

Adriaenssens, S., Block, P., Veenendaal, D., Williams, C., 2014. Shell Structures For architecture: form Finding and Optimization. Routledge.
Agarwal, D., Robinson, T.T., Armstrong, C.G., Kapellos, C., 2019. Enhancing CAD-based shape optimisation by automatically updating the CAD model's parameterisation. Struct. Multidiscip. Optim. 59, 1639–1654. https://doi.org/10.1007/s00158-018-2152-7.
Ansola, R., Canales, J., Tarrago, J.A., Rasmussen, J., 2004. Combined shape and reinforcement layout optimization of shell structures. Struct. Multidiscip. Optim. 27, 219–227. https://doi.org/10.1007/s00158-004-0399-7.
Ansola, R., Canales, J., Tarrago, J.A., Rasmussen, J., 2002. An integrated approach for shape and topology optimization of shell structures. Comput. Struct. 80, 449–458.
Antonau, I., Warnakulasuriya, S., Bletzinger, K.U., Bluhm, F.M., Hojjat, M., Wüchner, R., 2022. Latest developments in node-based shape optimization using vertex morphing parameterization. Struct. Multidiscip. Optim. 65. https://doi.org/10.1007/s00158-022-03279-w.
Bakker, C., Zhang, L., Higginson, K., Keulen, F.van, 2021. Simultaneous optimization of topology and layout of modular stiffeners on shells and plates. Struct. Multidiscip. Optim. 64, 3147–3161. https://doi.org/10.1007/s00158-021-03081-0.
Banigan, E.J., Stephens, A.D., Marko, J.F., 2017. Mechanics and buckling of biopolymeric shells and cell nuclei. Biophys. J. 113, 1654–1663. https://doi.org/10.1016/j.bpj.2017.08.034.
Bischoff, M., Bletzinger, K.U., Wall, W.A., Ramm, E., 2004. Models and finite elements for thin-walled structures. Encyclopedia of Computational Mechanics. Wiley. https://doi.org/10.1002/0470091355.ecm026.
Cai, S., Zhang, H., Zhang, W., 2023. An integrated design approach for simultaneous shape and topology optimization of shell structures. Comput. Methods Appl. Mech. Engrg. 415. https://doi.org/10.1016/j.cma.2023.116218.
Chapelle, D., Bathe, K.J., 2011. The Finite Element Analysis of shells: Fundamentals. Springer.
Cheng, K.T., Olhoff, N., 1981. An investigation concerning optimal design of solid elastic plates. Int. J. Solids Struct. 17, 305–323.
Choi, K.K., Kim, N.H., 2004. Structural Sensitivity Analysis and Optimization 1: Linear Systems. Springer Science & Business Media.
Cui, T., Du, Z., Liu, C., Sun, Z., Guo, X., 2022. Explicit topology optimization with moving morphable component (MMC) Introduction mechanism. Acta Mech. Solida Sin. 35, 384–408. https://doi.org/10.1007/s10338-021-00308-x.
Dey, T.K., Li, K., Sun, J., Cohen-Steinen, D., 2008. Computing geometry-aware handle and tunnel loops in 3D models. In: SIGGRAPH'08: International Conference on Computer Graphics and Interactive Techniques, ACM SIGGRAPH 2008 Papers 2008. https://doi.org/10.1145/1399504.1360644.
Dorn, C., Kochmann, D.M., 2023. Conformally graded metamaterials for elastic wave guidance. Extreme Mech. Lett. 65. https://doi.org/10.1016/j.eml.2023.102091.
Faber, J.A., Udani, J.P., Riley, K.S., Studart, A.R., Arrieta, A.F., 2020. Dome-patterned metamaterial sheets. Advanced Science 7. https://doi.org/10.1002/advs.202001955.
Feng, S., Wang, W., Wang, S., Cui, X., Yang, Y., Xu, F., Liu, L., Xu, Z., 2023. Controlling and visualizing fracture of 2D crystals by wrinkling. J. Mech. Phys. Solids 174. https://doi.org/10.1016/j.jmps.2023.105253.
Feng, S., Zhang, W., Meng, L., Xu, Z., Chen, L., 2021. Stiffener layout optimization of shell structures with B-spline parameterization method. Struct. Multidiscip. Optim. 63, 2637–2651. https://doi.org/10.1007/s00158-021-02873-8.
Gordon, V.D., Chen, X., Hutchinson, J.W., Bausch, A.R., Marquez, M., Weitz, D.A., 2004. Self-assembled polymer membrane capsules inflated by osmotic pressure. J. Am. Chem. Soc. 126, 14117–14122. https://doi.org/10.1021/ja0474749.
Gu, X., Wang, Y., Chan, T.F., Thompson, P.M., Yau, S.T., 2004. Genus zero surface conformal mapping and its application to brain surface mapping. In: IEEE Transactions on Medical Imaging, pp. 949–958. https://doi.org/10.1109/TMI.2004.831226.
Guo, X., Zhang, W., Zhong, W., 2014. Doing topology optimization explicitly and geometrically-a new moving morphable components based framework. J. Appl. Mech. 81. https://doi.org/10.1115/1.4027609.
Hao, P., Wang, B., Li, G., Meng, Z., Tian, K., Tang, X., 2014. Hybrid optimization of hierarchical stiffened shells based on smeared stiffener method and finite element method. Thin Wall Struct 82, 46–54. https://doi.org/10.1016/j.tws.2014.04.004.
Hassani, B., Tavakkoli, S.M., Ghasemnejad, H., 2013. Simultaneous shape and topology optimization of shell structures. Struct. Multidiscip. Optim. 48, 221–233. https://doi.org/10.1007/s00158-013-0894-9.
Hojjat, M., Stavropoulou, E., Bletzinger, K.U., 2014. The vertex morphing method for node-based shape optimization. Comput. Methods Appl. Mech. Engrg. 268, 494–513. https://doi.org/10.1016/j.cma.2013.10.015.
Huo, W., Liu, C., Du, Z., Jiang, X., Liu, Z., Guo, X., 2022. Topology optimization on complex surfaces based on the moving morphable component method and computational conformal mapping. J. Appl. Mech. 89. https://doi.org/10.1115/1.4053727.
Huo, W., Liu, C., Liu, Y., Du, Z., Zhang, W., Guo, X., 2023. A novel explicit design method for complex thin-walled structures based on embedded solid moving morphable components. Comput. Methods Appl. Mech. Engrg. 417. https://doi.org/10.1016/j.cma.2023.116431.
Jiang, X., Huo, W., Liu, C., Du, Z., Zhang, X., Li, X., Guo, X., 2023. Explicit layout optimization of complex rib-reinforced thin-walled structures via computational conformal mapping (CCM). Comput. Methods Appl. Mech. Engrg. 404. https://doi.org/10.1016/j.cma.2022.115745.
Jiang, X., Liu, C., Du, Z., Huo, W., Zhang, X., Liu, F., Guo, X., 2022. A unified framework for explicit layout/topology optimization of thin-walled structures based on Moving Morphable Components (MMC) method and adaptive ground structure approach. Comput. Methods Appl. Mech. Eng. 396. https://doi.org/10.1016/j.cma.2022.115047.
Jin, M., Kim, J., Luo, F., Gu, X., 2008. Discrete surface Ricci flow. IEEE Trans Vis Comput Graph 14, 1030–1043. https://doi.org/10.1109/TVCG.2008.57.
Kang, P., Youn, S.K., 2016. Isogeometric shape optimization of trimmed shell structures. Struct. Multidiscip. Optim. 53, 825–845. https://doi.org/10.1007/s00158-015-1361-6.
Kharevych, L., Springborn, B., Schröder, P., 2006. Discrete conformal mappings via circle patterns. ACM Trans. Graphics (TOG) 25, 412–438.
Kreisselmeier, G., Steinhauser, R., 1980. Systematic control design by optimizing a vector performance index. Computer Aided Design of Control Systems. Elsevier, pp. 113–117. https://doi.org/10.1016/b978-0-08-024488-4.50022-x.

Kuo, Y.C., Lin, W.W., Yueh, M.H., Yau, S.T., 2021. Convergent conformal energy minimization for the computation of disk parameterizations. SIAM J. Imaging Sci. 14, 1790–1815.
Lazarus, A., Florijn, H.C.B., Reis, P.M., 2012. Geometry-induced rigidity in nonspherical pressurized elastic shells. Phys. Rev. Lett. 109. https://doi.org/10.1103/PhysRevLett.109.144301.
Lim, G., Wortis, M., Mukhopadhyay, R., 2002. Stomatocyte-discocyte-echinocyte sequence of the human red blood cell: evidence for the bilayer-couple hypothesis from membrane mechanics. Proc. Natl. Acad. Sci. USA 99 (26), 16766–16769.
Liu, M., Zhen, Y., Sun, Y., He, L., Wu, K., Ni, Y., 2023. Universal shielding effect of curvature on two interacting cracks. J. Mech. Phys. Solids 179. https://doi.org/10.1016/j.jmps.2023.105389.
Liu, S., Li, Q., Chen, W., Hu, R., Tong, L., 2015. H-DGTP—A Heaviside-function based directional growth topology parameterization for design optimization of stiffener layout and height of thin-walled structures. Struct. Multidiscip. Optim. 52, 903–913. https://doi.org/10.1007/s00158-015-1281-5.
Lui, L.M., Lam, K.C., Wong, T.W., Gu, X., 2013. Texture map and video compression using Beltrami representation. SIAM J. Imaging Sci. 6, 1880–1902. https://doi.org/10.1137/120866129.
Lui, L.M., Lam, K.C., Yau, S.T., Gu, X., 2014. Teichmüller mapping (T-Map) and its applications to landmark matching registration. SIAM J. Imaging Sci. 7, 391–426. https://doi.org/10.1137/120900186.
Maute, K., Ramm, E., 1997. Adaptive topology optimization of shell structures. AIAA J 35, 1767–1773.
Meng, T.W., Choi, G.P.T., Lui, L.M., 2016. TEMPO: feature-endowed teichmüller extremal mappings of point clouds. SIAM J. Imaging Sci. 9, 1922–1962. https://doi.org/10.1137/15M1049117.
Mitchell, N.P., Koning, V., Vitelli, V., Irvine, W.T.M., 2017. Fracture in sheets draped on curved surfaces. Nat. Mater. 16, 89–93. https://doi.org/10.1038/nmat4733.
Piegl, L., Tiller, W., 2012. The NURBS Book. Springer Science & Business Media.
Pinkall, U., Polthier, K., 1993. Computing discrete minimal surfaces and their conjugates. Exp. Math. 2, 15–36.
Pisacane, V.L., 2005. Fundamentals of Space Systems, Second ed. Oxford University Press.
Shimoda, M., Liu, Y., 2014. A non-parametric free-form optimization method for shell structures. Struct. Multidiscip. Optim. 50, 409–423. https://doi.org/10.1007/s00158-014-1059-1.
Sokolowski, J., Zolesio, J.P., 1992. Introduction to Shape Optimization. Springer Berlin Heidelberg. https://doi.org/10.1007/978-3-642-58106-9.
Su, K., Cui, L., Qian, K., Lei, N., Zhang, J., Zhang, M., Gu, X.D., 2016. Area-preserving mesh parameterization for poly-annulus surfaces based on optimal mass transportation. Comput. Aided Geom. Des. 46, 76–91. https://doi.org/10.1016/j.cagd.2016.05.005.
Svanberg, K., 1987. The method of moving asymptotes—A new method for structural optimization. Int. J. Numer. Meth Eng. 24, 359–373. https://doi.org/10.1002/nme.1620240207.
Taubin, G., 1995. Estimating the tensor of curvature of a surface from a polyhedral approximation. In: IEEE International Conference on Computer Vision. IEEE, pp. 902–907. https://doi.org/10.1109/iccv.1995.466840.
Townsend, S., Kim, H.A., 2019. A level set topology optimization method for the buckling of shell structures. Struct. Multidiscip. Optim. 60, 1783–1800. https://doi.org/10.1007/s00158-019-02374-9.
Vitelli, V., Lucks, J.B., Nelson, D.R., 2006. Crystallography on curved surfaces. Proc. Natl. Acad. Sci. USA 103 (33), 12323–12328.
Wang, D., Abdalla, M.M., Wang, Z.P., Su, Z., 2019. Streamline stiffener path optimization (SSPO) for embedded stiffener layout design of non-uniform curved grid-stiffened composite (NCGC) structures. Comput. Methods Appl. Mech. Engrg. 344, 1021–1050. https://doi.org/10.1016/j.cma.2018.09.013.
Wu, D., Zhao, Z., Gao, H., 2024. An interface-enhanced discrete element model (I-DEM) of bio-inspired flexible protective structures. Comput. Methods Appl. Mech. Engrg. 420. https://doi.org/10.1016/j.cma.2023.116702.
Xiong, Y., Zhao, Z.L., Lu, H., Shen, W., Xie, Y.M., 2023. Parallel BESO framework for solving high-resolution topology optimisation problems. Adv. Eng. Softw. 176, 103389. https://doi.org/10.1016/j.advengsoft.2022.103389.
Xu, S., Jahn, W., Müller, J.D., 2014. CAD-based shape optimisation with CFD using a discrete adjoint. Int. J. Numer. Meth. Fl. 74, 153–168. https://doi.org/10.1002/fld.3844.
Zhang, W., Yuan, J., Zhang, J., Guo, X., 2016. A new topology optimization approach based on moving morphable components (MMC) and the ersatz material model. Struct. Multidiscip. Optim. 53, 1243–1260. https://doi.org/10.1007/s00158-015-1372-3.
Zhang, Y., Lai, X., Zhu, P., Wang, W., 2006. Lightweight design of automobile component using high strength steel based on dent resistance. Mater. Design 27, 64–68. https://doi.org/10.1016/j.matdes.2004.09.010.